






## Article

# Ground-Based RFI Source Localization via Single-Channel SAR Using Pulse Range Difference of Arrival

Jiaxin Wan <sup>1,2,3,4</sup> , Bing Han <sup>1,2,3,4,\*</sup>, Jianbing Xiang <sup>1,2</sup>, Di Yin <sup>1,2,3,4</sup>, Shangyu Zhang <sup>1,5</sup> , Jiazhi He <sup>1,5</sup> , Jiayuan Shen <sup>1,2,3</sup>  and Yugang Feng <sup>1,2</sup> 

<sup>1</sup> Aerospace Information Research Institute, Chinese Academy of Sciences, Beijing 100094, China; wanjiaxin22@mailsucas.ac.cn (J.W.); xiangjb@aircas.ac.cn (J.X.); yindi171@mailsucas.ac.cn (D.Y.); zhangsy01@aircas.ac.cn (S.Z.); hejz@aircas.ac.cn (J.H.); shenjiayuan20@mailsucas.ac.cn (J.S.); fengyugang21@mailsucas.ac.cn (Y.F.)

<sup>2</sup> Key Laboratory of Technology in Geo-Spatial Information Processing and Application System, Chinese Academy of Sciences, Beijing 100190, China

<sup>3</sup> School of Electronic, Electrical and Communication Engineering, University of Chinese Academy of Sciences, Beijing 100049, China

<sup>4</sup> Key Laboratory of Target Cognition and Application Technology, Beijing 100094, China

<sup>5</sup> Research Department of Cyber-Electromagnetic Space Information Technology, Chinese Academy of Sciences, Beijing 100094, China

\* Correspondence: han\_bing@mail.ie.ac.cn; Tel.: +86-010-5888-7208 (ext. 8956)

**Abstract:** Radio Frequency Interference (RFI) significantly degrades the quality of spaceborne Synthetic Aperture Radar (SAR) images, and RFI source localization is a crucial component of SAR interference mitigation. Single-station, single-channel SAR, referred to as single-channel SAR, is the most common operational mode of spaceborne SAR. However, studies on RFI source localization for this system are limited, and the localization accuracy remains low. This paper presents a method for locating the ground-based RFI source using spaceborne single-channel SAR echo data. First, matched filtering is employed to estimate the range and azimuth times of the RFI pulse-by-pulse in the SAR echo domain. A non-convex localization model using Pulse Range Difference of Arrival (PRDOA) is established based on the SAR observation geometry. Then, by applying Weighted Least Squares and Semidefinite Relaxation, the localization model is transformed into a convex optimization problem, allowing for the solution of its global optimal solution to achieve RFI source localization. Furthermore, the error analysis on the PRDOA localization model is conducted and the Cramér–Rao Lower Bound is derived. Based on the simulation platform and the SAR level-0 raw data of Gaofen-3, we conduct several verification experiments, with the Pulse Time of Arrival localization selected for comparison. The results demonstrate that the proposed method achieves localization accuracy with a hundred-meter error in azimuth and a kilometer-level total error, with the total localization errors reduced to approximately 1/4 to 1/3 of those of the Pulse Time of Arrival method.

**Keywords:** interference source localization; single-channel localization; radio frequency interference (RFI); synthetic aperture radar (SAR); parameter estimation; semidefinite relaxation (SDR)



Academic Editor: Fabio Rocca

Received: 3 December 2024

Revised: 27 January 2025

Accepted: 6 February 2025

Published: 8 February 2025

**Citation:** Wan, J.; Han, B.; Xiang, J.; Yin, D.; Zhang, S.; He, J.; Shen, J.; Feng, Y. Ground-Based RFI Source

Localization via Single-Channel SAR Using Pulse Range Difference of Arrival. *Remote Sens.* **2025**, *17*, 588. <https://doi.org/10.3390/rs17040588>

**Copyright:** © 2025 by the authors.

Licensee MDPI, Basel, Switzerland.

This article is an open access article distributed under the terms and conditions of the Creative Commons Attribution (CC BY) license (<https://creativecommons.org/licenses/by/4.0/>).

## 1. Introduction

Spaceborne Synthetic Aperture Radar (SAR) is an active microwave remote sensing device that has gained popularity due to its all-weather high-resolution imaging capabilities [1–3]. However, spectrum resources become scarce with technological advancements

and the continuous emergence of various electronic devices, such as ground-based radar stations, airport weather radar, and other terrestrial radiation sources. As a result, more and more radiation sources operate within the same frequency band as SAR, making spaceborne SAR susceptible to receiving Radio Frequency Interference (RFI), which seriously affects the quality of SAR imaging and interpretation [4–6]. Figure 1 presents examples of three spaceborne SAR images generated under RFI contamination.

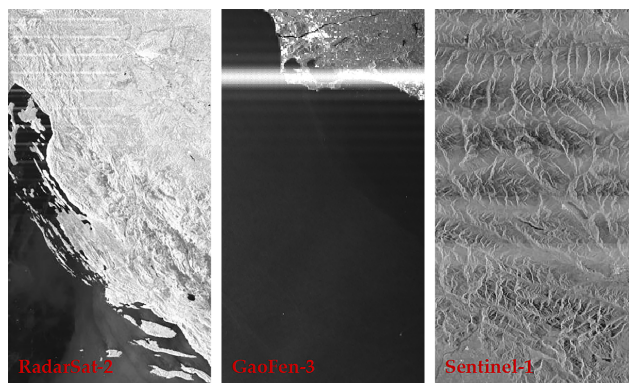


**Figure 1.** Examples of SAR images affected by RFI.

SAR RFI mitigation methods are mainly classified into RFI suppression and active interference mitigation. RFI suppression algorithms filter out RFI by analyzing the differences between the RFI signal and the SAR's echo in both time and frequency domains [7]. However, RFI suppression cannot guarantee that spaceborne SAR will not be repeatedly interfered by the same RFI sources, and each processing may result in the loss of some echo. In contrast, active interference mitigation uses practical methods with the received RFI signals, such as RFI source localization, to obtain the target characteristics of the RFI sources, then utilizing the beamforming techniques for spatial filtering, thereby reducing the RFI signals received by SAR [8,9]. Consequently, RFI source localization is critical for active interference mitigation in SAR systems, and plays a vital role in spaceborne SAR interference mitigation.

Using spaceborne SAR for RFI source localization falls under the passive localization methods. Current passive localization methods are generally divided into two-step localization and direct localization. To date, researchers have proposed various passive two-step localization methods that utilize parameters for localization, such as Direction of Arrival (DOA) [10], Time Difference of Arrival (TDOA) [11], and so on. For example, Dogancay [12] proposed the Total Least Squares algorithm to solve the DOA localization problem. Chan and Ho [13] introduced a two-step Weighted Least Squares algorithm for TDOA localization. Direct localization methods construct a received signal model and combine it with actual signals for localization, which can achieve higher precision than two-step localization under specific conditions [14]. Wang et al. [15] applied the synthetic aperture technique to signal source localization, addressing the dependence of traditional direct localization on antenna arrays. However, these methods require sensors to continuously receive signals, which contradicts the requirement for SAR platforms to possess transmitting and receiving windows simultaneously.

Various algorithms to address the problem of RFI source localization based on spaceborne SAR are proposed. Dan [16] introduced the concept of the X-mark using observations from ascending and descending passes to locate RFI sources. Leng et al. [17] demonstrated that the X-mark method has spatial accuracy within a rhombic area of 89 square kilometers and utilized this method to locate RFI sources in Sentinel-1 images. However, the assumption of continuous RFI presence is required to be achieved when using the X-mark method.

Yu et al. [18] proposed an RFI source localization method based on dual-channel SAR, where phase shifts caused by the time differences of RFI signal arrival across channels are used to locate the RFI source. However, this method requires the RFI signal to be significantly more powerful than the spaceborne SAR echo. Lin et al. [19] and Yu et al. [20] estimated the DOA of RFI sources at different azimuth moments in multi-channel SAR systems, achieving localization accuracy at the kilometer level. However, this method requires the phase center distance between SAR channels to be greater than half the wavelength of the RFI signal, which may cause angular ambiguity when applying the DOA method. Thus, it is evident that the methods mentioned before have limited accuracy in locating ground-based RFI sources. These methods also require the SAR system to be equipped with multiple receiving antennas for DOA and other parameter estimations, thus not applying to single-station, single-channel SAR RFI source localization (hereinafter referred to as single-channel SAR), which remains the most common configuration in spaceborne SAR systems. Therefore, the applicability of these methods is constrained.

Current research on RFI source localization for single-channel SAR is limited. Yang et al. [21] introduced an RFI source localization method based on Pulse Time of Arrival (PTOA) and achieved favorable simulation results. However, this method has stringent accuracy requirements for estimating PTOA and its first- and second-order Taylor series coefficients, which can lead to error iteration effects and significantly degrade localization accuracy. Zhou et al. [22] built upon the PTOA concept to design a grid-search RFI localization method based on TDOA, suitable for single-channel SAR with single or multiple passes. The method was validated using two sets of single-channel observation data from the GaoFen-3 (GF3) satellite in the same observation region. The results showed a localization error of only 3.708 km, although the error for a single measurement could exceed 100 km because of ignoring the pulse repetition interval (PRI) of the RFI signal. In summary, existing methods for RFI localization using single-channel SAR exhibit limitations.

This paper proposes a spaceborne single-channel SAR RFI source localization method based on the Pulse Range Difference of Arrival (PRDOA). First, matched filtering is employed to estimate the reception times of the RFI pulses in the SAR echo domain. By calculating the PRDOA, a non-convex likelihood function containing the RFI source location is constructed. The Maximum Likelihood Estimation (MLE) is approximated as a convex optimization problem using Weighted Least Squares (WLS) and Semidefinite Relaxation (SDR) for solving. The bias, covariance, and Cramér–Rao Lower Bound (CRLB) of the PRDOA localization model are derived. Simulations and experimental validations using GF3 data with RFI are conducted to analyze the localization accuracy of the proposed method under various conditions. Compared with the PTOA localization in reference [21], the results show that the overall positioning accuracy of the proposed algorithm improves by a factor of 3 to 4.

The main contributions of this paper are summarized as follows:

- A pulse-level estimation algorithm for the azimuth and range times of RFI signals in the SAR echo domain is proposed, enabling accurate RFI signal timing information estimation in the SAR echo domain.
- A mathematical model relating PRDOA to the RFI source location is established, and semidefinite relaxation techniques are applied. By incorporating prior information from SAR observations, the non-convex localization model is relaxed into a convex optimization problem, simplifying the localization process and ensuring the algorithm's stability while achieving optimal solutions.
- Simulation experiments are designed for spaceborne single-channel SAR and ground-based RFI source localization, complemented by empirical validation using GF3 SAR Level-0 raw data. The results indicate that under single-channel SAR observation,

the PRDOA localization model achieves kilometer-level total accuracy and meter-level azimuth accuracy. Additionally, the model successfully locates the potential RFI source from RFI-contaminated GF3 raw echo data, further validating the applicability of the proposed method to spaceborne single-channel SAR.

The rest of this paper is organized as follows: Section 2 introduces the geometric relationship between the single-channel SAR and the RFI source, along with the RFI signal model. Section 3 presents the azimuth and range time estimation algorithms for RFI pulse-level processing in the SAR echo domain and the single-channel SAR RFI source localization method based on PRDOA and SDR, analyzing the performance of the proposed method in detail. Subsequently, Section 4 conducts simulation experiments and validation using real data. Section 5 discusses the experimental results, considering the algorithm's limitations and potential future works. Finally, Section 6 concludes the paper.

The following notations are adopted throughout this paper. Boldface lowercase and boldface uppercase letters denote the vectors and matrices, respectively.  $*^o$  denotes the theoretical value of the parameter.

## 2. Geometric Relationship and Signal Model

For spaceborne SAR systems, most RFI sources are related to electronic devices on the Earth's surface [23]. Therefore, this paper focuses on establishing a spatial geometric model of spaceborne SAR affected by the ground-based RFI source. It should be noted that, unless otherwise specified, all geographical coordinates in this paper are based on the Earth-Centered Earth-Fixed (ECEF) coordinate system. Figure 2 illustrates the spatial relationships between the three-dimensional coordinates in the ECEF system, the Earth's equator, the Greenwich meridian, and the geometric model between the SAR system and the RFI source when it simultaneously receives real echoes and RFI signals.

The derivation of the proposed algorithm is based on the following two fundamental assumptions:

- A1 The satellite trajectory measurement errors are negligible.
- A2 The RFI signals have been detected, and the parameter estimation of RFI is reasonably accurate.

The trajectory measurement error of a satellite is determined by orbit determination technology. Current orbit determination techniques indicate that, regardless of the satellite's orbital altitude, the ratio of satellite trajectory measurement error to satellite coordinates is only  $10^{-9}$  to  $10^{-6}$  [24–26]. Consequently, the real-time coordinate errors of spaceborne single-channel SAR satellites can be regarded as negligible, ensuring the validity of Assumption A1.

During the data acquisition, the SAR satellite moves in an elliptical orbit, with the antenna pointing towards the imaging area on the flight direction side. The variation in the satellite coordinates over time can be expressed as follows:

$$\mathbf{s}(t) = \mathbf{a}t^2 + \mathbf{b}t + \mathbf{c} \quad (1)$$

Here,  $\mathbf{s}(t) = (x_s, y_s, z_s)^T$  represents the coordinates of the satellite as a function of time  $t$ .  $\mathbf{a}$ ,  $\mathbf{b}$ , and  $\mathbf{c}$  are three-dimensional column vectors that denote the coefficients of a second-order polynomial in time  $t$ , determined by the satellite's six orbital elements.

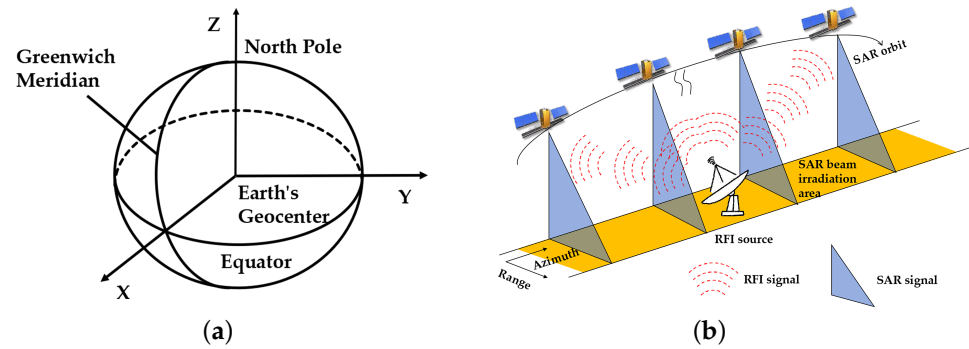


**Figure 2.** Schematic diagram of the ECEF coordinate system and the geometric relationship between SAR and RFI sources: (a) ECEF coordinate system; (b) Geometric relationship between SAR and the RFI source.

A stationary ground-based RFI source is located within the SAR imaging area, with coordinates  $\mathbf{u} = (x, y, z)^T$ . The emitted signal can be expressed as:

$$rfi_{send}(t^t) = \sum_{n=0}^{+\infty} \text{rect}\left(\frac{t^t - nT_n^o}{T_{pn}^o}\right) e^{j\varphi(t^t - nT_n^o)} e^{j\omega_c \cdot (t^t - nT_n^o)} \quad (2)$$

Here,  $\text{rect}()$  denotes the rectangular window of the RFI signal,  $t^t$  represents the emission time of the RFI signal,  $n$  indicates the pulse sequence number emitted by the RFI source,  $T_n^o$  is the PRI for the  $n$ th pulse from the RFI source and  $T_{pn}^o$  is the pulse width of the  $n$ th RFI pulse,  $e^{j\omega_c \cdot (t^t)}$  is the carrier frequency of the signal, and  $e^{j\varphi(t^t)}$  is the modulation phase. The emission time of the  $n$ th pulse can be expressed as:

$$t_n^{to} = t_0^{to} + \sum_{i=0}^n T_i^o \quad (3)$$

where  $t_n^{to}$  and  $t_0^{to}$  represent the emission times of the  $n$ th and 0th RFI pulses, respectively. When the spaceborne SAR passes over the RFI source, the signals received by the SAR exist in the two-dimensional time domain, which can be expressed as follows:

$$x(\tau, \eta) = rfi_{receive}(\tau, \eta) + echo(\tau, \eta) + noise(\tau, \eta) \quad (4)$$

where  $\tau$  is the range time in the SAR echo domain,  $\eta$  is the azimuth time in the SAR echo domain,  $rfi_{receive}$  represents the received RFI signal,  $echo$  denotes the scattered signal from the SAR, and  $noise$  indicates the received noise signal. The model of the received RFI signal can be expressed as follows:

$$\begin{aligned} rfi_{receive}(\tau, \eta) &= \sum_{n=0}^N A(\eta) \text{rect}\left(\frac{\tau + \eta - nT_n^o}{T_{pn}^o}\right) e^{j\varphi(\tau + \eta - nT_n^o)} e^{j\omega_c \cdot (\tau + \eta - nT_n^o)} \\ &= \sum_{n=0}^N A(\eta) \text{rect}\left(\frac{t^t - nT_n^o - d_n}{T_{pn}^o}\right) e^{j\varphi(t^t - nT_n^o - d_n)} e^{j\omega_c \cdot (t^t - nT_n^o - d_n)} \end{aligned} \quad (5)$$

Here,  $A(\eta)$  is the antenna pattern of the RFI source,  $N$  is the number of RFI signal pulses received by the SAR, and  $d_n$  is the one-way slant range delay of the  $n$ th pulse, which is related to the position  $\mathbf{u}$  of the RFI source, expressed as follows:

$$d_n = \frac{\|\mathbf{u} - \mathbf{s}_n\|}{c} = \frac{R_n^{ro}}{c} \quad (6)$$

where  $R_n^{ro}$  is the slant range of the  $n$ th RFI pulse,  $\mathbf{s}_n$  is the position coordinates of the platform when the SAR receives the  $n$ th RFI pulse.  $d_n$  and  $t_n^{to}$  influence the reception time of the  $n$ th RFI pulse by the SAR, represented as follows:

$$\tau_n^o + \eta_n^o = t_n^{to} + d_n (n = 0, 1, 2 \dots, N) \quad (7)$$

where  $\tau_n^o$  and  $\eta_n^o$  represent the range and azimuth times when the SAR receives the  $n$ th RFI pulse. Therefore, the position of the RFI source can be inverted using Equation (7).

Due to the relatively small signal energy loss caused by the one-way slant range, the power of the RFI signal is usually greater than that of the SAR scattered echo, making the RFI characteristics very pronounced in the echo domain. Therefore, based on the different characteristics of the RFI signal and the SAR scattered signal in the echo domain, it is possible to detect the presence of RFI frame-by-frame and perform parameter estimation and modulation type classification. The corresponding azimuth time  $\eta$  of each RFI pulse can be calculated.

Existing RFI detection and parameter estimation techniques can leverage deep learning networks and iterative adaptive methods to ensure a detection rate of 91% for interference signals, with parameter estimation errors of the order of  $10^{-2}$ , achieving a high detection rate and low estimation error [27–29]. This paper selects references [27,28] to achieve relatively accurate RFI detection and parameter estimation, thereby ensuring the validity of Assumption A2.

### 3. Single-Channel SAR RFI Source Localization Model Based on PRDOA

In this section, we first design an algorithm for estimating the azimuth and range time of RFI pulses in the SAR echo domain based on the geometric and signal model proposed in Section 2, which serves as the foundation for constructing the PRDOA model, with parameters including the RFI source position  $\mathbf{u}$ . By inverting the PRDOA model, we achieve RFI source localization and simplify the inversion complexity using SDR techniques.

#### 3.1. Pulse-by-Pulse Time Estimation of RFI Signals in the SAR Echo Domain

Traditional algorithms for estimating signal-time information mainly rely on extracting the signal envelope and estimating its rising and falling edges [30]. However, the scattered echo and noise received by SAR can interfere with extracting the RFI signal envelope. To address this, we use matched filtering combined with RFI detection and parameter estimation to improve the accuracy of range and azimuth time estimation for each RFI pulse.

The frame containing the RFI signal, signal parameters, and modulation type can be identified through RFI signal detection and parameter estimation. Additionally, the azimuth time  $\eta$  for all RFI pulses within the current frame, as received by the SAR, can be estimated. For estimating the range time  $\tau$ , we construct the RFI single pulse reference signal using the result of RFI's parameter estimation:

$$rfi_{refer}(t) = \text{rect}\left(\frac{-t}{T_p^o}\right) e^{-j\varphi(-t)} e^{j\omega_c \cdot t} \quad (8)$$

where  $T_p^o$  is the pulse width of the reference signal. The matched filtering is achieved by convolving Equation (5) with Equation (8). The result is shown in Equation (9). This process concentrates the energy of each RFI pulse at the pulse center, forming multiple sharp peak signals.

$$rfi_{compression}(\tau, \eta) = \sum_{n=0}^I \text{sinc}(\tau + \eta - nT_n^o) e^{j\omega_c \cdot (\tau + \eta - nT_n^o)} \quad (9)$$

The center time of each pulse is delayed by half of the pulse width in the range time compared to when it is received. Thus, the range-time estimation of RFI pulses in the SAR echo domain can be expressed as shown in Equation (10). By incorporating the results of RFI detection, the azimuth and range time information of RFI pulses in the SAR echo domain can be obtained.

$$\tau_n^o = t_{peakn}^o - \frac{T_{pn}^o}{2} \quad (10)$$

where  $t_{peakn}^o$  represents the peak time of the  $n$ th RFI pulse after matched filtering, which corresponds to the center time of the  $n$ th pulse.

To validate the proposed method's capability to accurately estimate the range times of RFI signal pulses with different modulation types under the influence of other signals received by SAR, simulations are conducted for two typical modulation types, linear frequency modulation (LFM) and sinusoidal frequency modulation, and range time estimation is performed. A low signal-to-noise ratio (SNR) is set to simulate the influence of non-RFI signals, with the SNR set to  $-10$  dB, and the range times of the simulated signals are identical across different modulation types. Figure 3 presents the processing results in both the time and time-frequency domains.

As shown in Figure 3a, the simulated signals are nearly indistinguishable from noise under an SNR of  $-10$  dB. Figure 3b,c indicate that the pulse energy of different modulation types is concentrated at their respective central moments which can be accurately estimated after matched filtering. The peak times of each frame's signals are extracted, and  $\tau$  is calculated using Equation (10). The results show that the mean error between the estimated and theoretical range times of the RFI pulses within two frames is 2 ns, and the range time error between the two frames is 1 ns. This demonstrates that matched filtering enables accurate estimation of the range time  $\tau$ . Considering that LFM signals are among the most common modulation types used in terrestrial radiators, subsequent analyses focus mainly on the LFM signals.

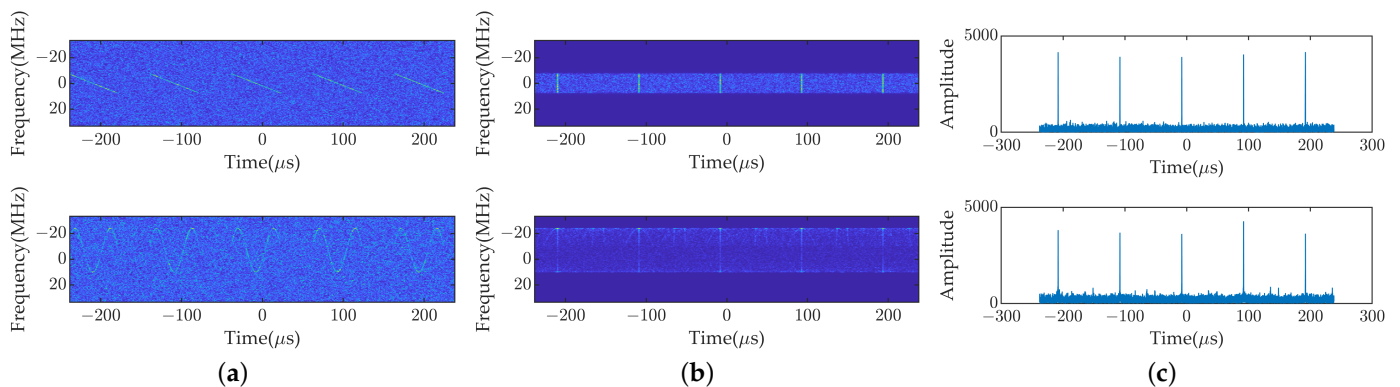


**Figure 3.** Representations of signals with different modulation (linear and sinusoidal frequency modulation) at an SNR of  $-10$  dB, along with the corresponding results after matched filtering: (a) Time-frequency domain image of the original signals; (b) Time-frequency domain image of the signals after matched filtering; (c) Time-domain amplitude plot of the signals after matched filtering.

In practical scenarios, certain RFI sources can emit interference signals with dynamic PRI and pulse width, resulting in incomplete reception of RFI pulses within the SAR receiving window and affecting the range time estimation. The characteristics of PRI and pulse width affecting the complete reception of RFI pulses can be summarized into the following three cases:

1. The PRI of RFI is less than the length of the SAR receiving window.

2. The PRI of RFI is greater than the length of the SAR receiving window while the pulse width is shorter than the SAR receiving window.
3. The pulse width of the RFI is longer than the SAR receiving window.

Case 3 serves as the sufficient condition for RFI pulses not being fully received. Assuming the  $n$ th RFI pulse satisfies case 3, the relationship between the pulse width  $T_{pn}^o$  and the length of the SAR receiving window is shown as follows:

$$\Delta T_n = T_{pn}^o - T_{SAR\_re} \quad (11)$$

Here,  $T_{SAR\_re}$  represents the length of the SAR receiving window, and  $\Delta T_n$  denotes the time by which the  $n$ th RFI pulse exceeds the receiving window length. An approximation is made to estimate the range time of the  $n$ th pulse: the received portion of the  $n$ th pulse is regarded as a new pulse  $n$ . After matched filtering, the relationship between the peak time of the new pulse and the peak time of the original pulse can be expressed as follows:

$$t_{peakn} = t_{peakn}^o - \frac{\Delta T_n}{2} + \Delta t_{peakn} \quad (12)$$

where  $t_{peakn}$  denotes the peak time of the  $n$ th RFI pulse after approximation, and  $\Delta t_{peakn}$  represents the offset noise caused by partial phase loss during matched filtering. Based on Equation (10), the relationship between the range time of the approximated  $n$ th pulse and the range time of the original pulse is given by:

$$\tau_n = t_{peakn} - \frac{T_{pn}^o - \Delta T_n}{2} = \tau_n^o + \Delta t_{peakn} \quad (13)$$

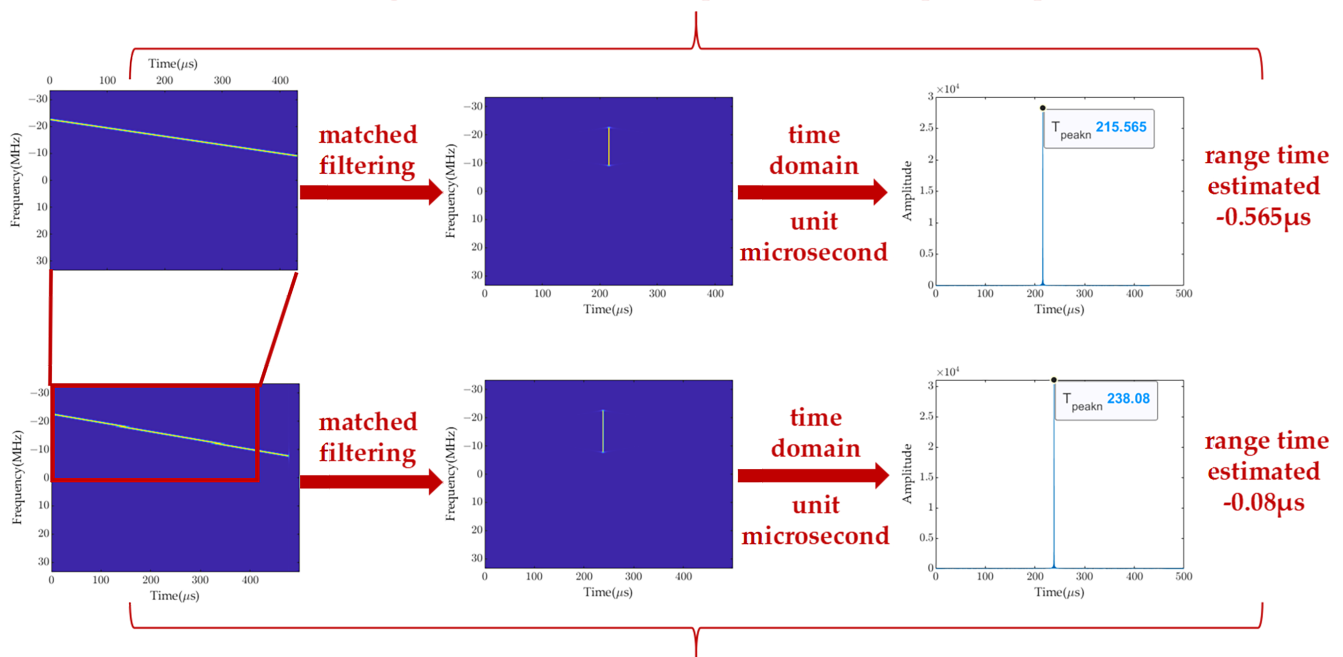
It is evident that, after approximation, the error in the range time estimation for the  $n$ th pulse is primarily caused by measurement noise introduced by phase loss. When the pulse's phase varies continuously and  $\Delta T_n$  is small, a well-designed matched filter for remain pulse can be made, making  $\Delta t_{peakn}$  negligible.

To validate the feasibility of the proposed approximation algorithm, a single-frame LFM signal with a pulse width of 476  $\mu$ s is simulated, and a window function is designed to simulate the retention of RFI signal pulses within the SAR receiving window. The lengths of the window function are set to 500  $\mu$ s and 430  $\mu$ s to obtain one frame of fully received and one frame of partially received signals, respectively. In this simulation, the arrival time of the RFI pulse is set to 0.

Figure 4 presents the processing flow and results of matched filtering and range time  $\tau$  estimation for the two frames of signals. The signal's time-frequency domain variations indicate that the energy focusing is achieved for both fully received and partially received pulses. Based on the signal peak time in the time-domain amplitude plot and Equations (10) and (13), the range time  $\tau$  is estimated for both frames. The results show that the  $\tau$  estimation for the partially received signal is close to that of the fully received signal and the true value. This demonstrates that approximating the partially received RFI pulses allows a relatively accurate estimation of their range time.



### The range time estimation for RFI pulse under incomplete reception



### The range time estimation for RFI pulse under complete reception

**Figure 4.** Processing steps and results of matched filtering and range time  $\tau$  estimation for fully and partially received LFM signals.

#### 3.2. RFI Source Localization Model Based on PRDOA

Combining Equations (6) and (7), the theoretical slant range corresponding to the  $n$ th pulse can be expressed as follows:

$$R_n^{ro} = c(\tau_n^o + \eta_n^o - t_n^{to}) \quad (n = 0, 1, 2 \dots, N) \quad (14)$$

Let the slant range of the 0th pulse be the reference. By combining Equation (3), the difference between the slant ranges of the other pulses and that of the reference gives the required PRDOA theoretical values, as follows:

$$R_{n0}^o = R_n^{ro} - R_0^{ro} = c \left[ \tau_n^o + \eta_n^o - (\tau_0^o + \eta_0^o) - \sum_{i=0}^{n-1} T_i^o \right] \quad (15)$$

In practical scenarios, due to errors in the estimation of the RFI signal parameters, there is a deviation between the time estimation results in Section 3.1 and  $\sum_{i=0}^{n-1} T_i$  compared to the theoretical values. Therefore, the PRDOA measurement corresponding to the  $n$ th pulse can be expressed as follows:

$$R_{n0} = R_{n0}^o + \Delta r_{n0} = c \left[ \tau_n + \eta_n - (\tau_0 + \eta_0) - \sum_{i=0}^{n-1} T_i \right] + \Delta r_{n0} \quad (16)$$

Here,  $\Delta r_{n0}$  is the measurement noise of PRDOA. Consequently, by utilizing Equation (16), the PRDOA measurement results for pulses from the first to the  $N$ th can be derived, allowing the organization of these PRDOA measurements into a vector Equation as follows:

$$\mathbf{R} = \mathbf{R}^o + \Delta \mathbf{r} \quad (17)$$

where  $\mathbf{R}$ ,  $\mathbf{R}^o$ , and  $\Delta \mathbf{r}$  are expressed as follows:

$$\begin{aligned}
\mathbf{R} &= [R_{10}, R_{20}, \dots, R_{N0}]^T \\
\mathbf{R}^o &= [R_{10}^o, R_{20}^o, \dots, R_{N0}^o]^T \\
\Delta \mathbf{r} &= [\Delta r_{10}, \Delta r_{20}, \dots, \Delta r_{N0}]^T
\end{aligned} \tag{18}$$

### 3.2.1. Maximum Likelihood Estimation

For analytical convenience, we assume that the measurement error  $\Delta \mathbf{r}$  of PRDOA follows a Gaussian distribution with a mean of 0 and a variance of  $\sigma_{PRDOA}^2$ . Consequently, the likelihood function based on PRDOA can be constructed for the MLE, which is equivalent to minimizing the following cost function:

$$\min_{\mathbf{u}} \left( \mathbf{R} - \mathbf{R}^o(\mathbf{u}) \right)^T \mathbf{Q}^{-1} \left( \mathbf{R} - \mathbf{R}^o(\mathbf{u}) \right) \tag{19}$$

where  $\mathbf{Q} = \sigma_{PRDOA}^2 \mathbf{V}_r$  represents the covariance matrix of PRDOA.  $\mathbf{V}_r$  is a square matrix with diagonal elements equal to 1 and other elements equal to 0.5. The curved trajectory of the spaceborne SAR will result in multiple optimal solutions for Equation (19). To obtain the desired RFI source localization results, it is necessary to introduce prior information about the RFI source as constraints. Generally, the ground-based RFI source is located within the swath of the SAR, allowing us to obtain the following prior information about RFI source location  $\mathbf{u}$ :

1. Each coordinate of  $\mathbf{u}$  falls within the coordinate ranges of the corners of the swath;
2. The slant range value of the RFI source is within the maximum and minimum slant range of the entire scene image;
3. The geocentric distance of the RFI source is within the Earth's radius range of the swath.

By organizing this prior information, we can establish the following constraints.

$$\begin{aligned}
x_{\min} &\leq \mathbf{u}(1) \leq x_{\max} \\
y_{\min} &\leq \mathbf{u}(2) \leq y_{\max} \\
z_{\min} &\leq \mathbf{u}(3) \leq z_{\max} \\
R_{near} &\leq \|\mathbf{u} - \mathbf{s}_{\eta_c}\| \leq R_{far} \\
ra_{scene} - \Delta ra &\leq \|\mathbf{u}\| \leq ra_{scene} + \Delta ra
\end{aligned} \tag{20}$$

Here,  $x_{\max}$ ,  $x_{\min}$ ,  $y_{\max}$ ,  $y_{\min}$ ,  $z_{\max}$ , and  $z_{\min}$  represent the maximum and minimum values of the three-dimensional coordinates of the corners of the swath,  $\mathbf{s}_{\eta_c}$  is the coordinate of the spaceborne SAR at the Doppler center corresponding to the RFI source, which can be determined by estimating the minimum PRDOA,  $ra_{scene}$  is the Earth's radius in the swath area, and  $\Delta ra$  represents fluctuations in the geocentric distance.

Therefore, by consolidating Equations (19) and (20), we construct the spaceborne single-channel SAR RFI source localization model based on PRDOA:

$$\begin{aligned}
&\min_{\mathbf{u}} \left( \mathbf{R} - \mathbf{R}^o(\mathbf{u}) \right)^T \mathbf{Q}^{-1} \left( \mathbf{R} - \mathbf{R}^o(\mathbf{u}) \right) \\
&s.t. x_{\min} \leq \mathbf{u}(1) \leq x_{\max} \\
&y_{\min} \leq \mathbf{u}(2) \leq y_{\max} \\
&z_{\min} \leq \mathbf{u}(3) \leq z_{\max} \\
&R_{near} \leq \|\mathbf{u} - \mathbf{s}_{\eta_c}\| \leq R_{far} \\
&ra_{scene} - \Delta ra \leq \|\mathbf{u}\| \leq ra_{scene} + \Delta ra
\end{aligned} \tag{21}$$

### 3.2.2. Weighted Least Squares Construction

The cost function in Equation (21) and the last two constraints are all non-convex, making it difficult to obtain a global optimal solution for the localization results. To address this, an SDR method is introduced to approximate the optimization problem in Equation (21). First, referring to reference [13], the cost function in Equation (21) is approximated using the WLS equation. Squaring both sides of the first equal sign in Equation (15) and incorporating measurement noise while neglecting the second-order noise terms yields the following:

$$R_{n0}^2 + 2R_{n0}R_0^{ro} - \|\mathbf{s}_n\|^2 + \|\mathbf{s}_0\|^2 + 2(\mathbf{s}_n - \mathbf{s}_0)^T \mathbf{u} = 2R_n^{ro} \Delta r_{n0} \quad (22)$$

Letting  $R_{n0}^o$  be an intermediate variable, a linear equation regarding the new variable  $\mathbf{x}_R = [\mathbf{u}^T, R_0^{ro}]^T$  can be derived and expressed in matrix form as follows:

$$\mathbf{A}_R \mathbf{x}_R - \mathbf{B}_R = \mathbf{C}_R \Delta \mathbf{r} \quad (23)$$

where,

$$\mathbf{A}_R = 2 \begin{bmatrix} (\mathbf{s}_1 - \mathbf{s}_0)^T & R_{20}^o \\ \vdots & \vdots \\ (\mathbf{s}_N - \mathbf{s}_0)^T & R_{N0}^o \end{bmatrix} \quad (24)$$

$$\mathbf{B}_R = - \begin{bmatrix} R_{10} - \mathbf{s}_1^T \mathbf{s}_1 + \mathbf{s}_0^T \mathbf{s}_0 \\ \vdots \\ R_{N0} - \mathbf{s}_N^T \mathbf{s}_N + \mathbf{s}_0^T \mathbf{s}_0 \end{bmatrix} \quad (25)$$

$$\mathbf{C}_R = 2 \text{diag} \{ R_1^{ro}, \dots, R_N^{ro} \} \quad (26)$$

Comparing Equations (17) and (23), we find the following:

$$\mathbf{C}_R^{-1} (\mathbf{A}_R \mathbf{x}_R - \mathbf{B}_R) \approx \Delta \mathbf{r} = \mathbf{R} - \mathbf{R}^o(\mathbf{u}) \quad (27)$$

Therefore, the PRDOA localization model in Equation (21) can be transformed into the following:

$$\begin{aligned} & \min_{\mathbf{x}_R} \left( \mathbf{C}_R^{-1} (\mathbf{A}_R \mathbf{x}_R - \mathbf{B}_R) \right)^T \mathbf{Q}^{-1} \left( \mathbf{C}_R^{-1} (\mathbf{A}_R \mathbf{x}_R - \mathbf{B}_R) \right) \\ & = \min_{\mathbf{x}_R} (\mathbf{A}_R \mathbf{x}_R - \mathbf{B}_R)^T \mathbf{Q}_{\mathbf{x}_R}^{-1} (\mathbf{A}_R \mathbf{x}_R - \mathbf{B}_R) \\ & \text{s.t. } \mathbf{x}_R(4) = \|\mathbf{x}_R(1:3) - \mathbf{s}_1^o\| \\ & x_{\min} \leq \mathbf{x}_R(1) \leq x_{\max} \\ & y_{\min} \leq \mathbf{x}_R(2) \leq y_{\max} \\ & z_{\min} \leq \mathbf{x}_R(3) \leq z_{\max} \\ & R_{near} \leq \|\mathbf{x}_R(1:3) - \mathbf{s}_{\eta_c}\| \leq R_{far} \\ & ra_{scene} - \Delta ra \leq \|\mathbf{x}_R(1:3)\| \leq ra_{scene} + \Delta ra \end{aligned} \quad (28)$$

Equation (28) transforms the MLE problem of PRDOA by neglecting the higher-order terms of the measurement error. Based on the estimation methods in Section 3.1 and Assumption A2, the time estimation error can be maintained at the ns level under lower signal-to-noise ratios, and the PRI of each RFI pulse can be accurately estimated, ensuring a high estimation accuracy of PRDOA. Therefore, Equation (28) can be considered equivalent to the RPDOA localization model in Equation (21).

In Equation (26),  $\mathbf{C}_R$  also includes the unknown variable  $[R_1^{ro}, \dots, R_N^{ro}]^T$ . According to reference [13], the impact of  $\mathbf{C}_R$  on Equation (28) is minor. Additionally, the RFI source is

located in the far field relative to the single-channel SAR, which means that the slant ranges between the targets in the swath and SAR are of the same order of magnitude. Therefore, to simplify the calculation, the slant range information at the center point of the swath is set as the initial value to substitute into  $\mathbf{C}_R$  for calculation.

### 3.2.3. Semidefinite Relaxation

Although the cost function and the last two constraints in Equation (28) remain non-convex, they involve norm or quadratic calculations, making it straightforward to apply the SDR method while ensuring that the optimal solution obtained is consistent with that of the PRDOA localization model in Equation (21). By introducing a new variable  $\mathbf{X}_R = \mathbf{x}_R \mathbf{x}_R^T$ , the cost function and the first constraint condition of Equation (28) can be transformed into the following:

$$\begin{aligned} \min_{\mathbf{X}_R, \mathbf{x}_R} \quad & \text{tr} \left\{ \begin{bmatrix} \mathbf{X}_R & \mathbf{x}_R \\ \mathbf{x}_R^T & \mathbf{1} \end{bmatrix} \mathbf{E}_R \right\} \\ \text{s.t. } \mathbf{X}_R(4,4) = & \text{tr}\{\mathbf{X}_R(1:3,1:3)\} - 2\mathbf{s}_0^T \mathbf{x}_R(1:3) + \mathbf{s}_0^T \mathbf{s}_0 \\ & \begin{bmatrix} \mathbf{X}_R & \mathbf{x}_R \\ \mathbf{x}_R^T & \mathbf{1} \end{bmatrix} \geq 0 \\ & \text{rank}(\mathbf{X}_R) = 1 \end{aligned} \quad (29)$$

where,

$$\mathbf{E}_R = \begin{bmatrix} \mathbf{A}_R^T \mathbf{Q}_{\mathbf{x}_R}^{-1} \mathbf{B}_R & -\mathbf{A}_R^T \mathbf{Q}_{\mathbf{x}_R}^{-1} \mathbf{B}_R \\ -\mathbf{B}_R^T \mathbf{Q}_{\mathbf{x}_R}^{-1} \mathbf{A}_R & \mathbf{B}_R^T \mathbf{Q}_{\mathbf{x}_R}^{-1} \mathbf{B}_R \end{bmatrix} \quad (30)$$

Except for the Rank-1 constraint, the cost function and the remaining constraints in Equation (29) are convex. By eliminating the Rank-1 constraint, we can transform Equation (29) into a convex Semidefinite Programming (SDP) model:

$$\begin{aligned} \min_{\mathbf{X}_R, \mathbf{x}_R} \quad & \text{tr} \left\{ \begin{bmatrix} \mathbf{X}_R & \mathbf{x}_R \\ \mathbf{x}_R^T & \mathbf{1} \end{bmatrix} \mathbf{E}_R \right\} \\ \text{s.t. } \mathbf{X}_R(4,4) = & \text{tr}\{\mathbf{X}_R(1:3,1:3)\} - 2\mathbf{s}_0^T \mathbf{x}_R(1:3) + \mathbf{s}_0^T \mathbf{s}_0 \\ & \begin{bmatrix} \mathbf{X}_R & \mathbf{x}_R \\ \mathbf{x}_R^T & \mathbf{1} \end{bmatrix} \geq 0 \end{aligned} \quad (31)$$

Moreover, we observe that, due to the introduction of the variable  $\mathbf{X}_R$ , the constraints in Equation (20) are transformed into the following:

$$\begin{aligned} x_{\min} & \leq \mathbf{x}_R(1) \leq x_{\max} \\ y_{\min} & \leq \mathbf{x}_R(2) \leq y_{\max} \\ z_{\min} & \leq \mathbf{x}_R(3) \leq z_{\max} \\ R_{near}^2 & \leq \text{tr}\{\mathbf{X}_R(1:3,1:3)\} - 2\mathbf{s}_{\eta_c}^T \mathbf{x}_R(1:3) + \mathbf{s}_{\eta_c}^T \mathbf{s}_{\eta_c} \leq R_{far}^2 \\ (ra_{scene} - \Delta ra)^2 & \leq \text{tr}\{\mathbf{X}_R(1:3,1:3)\} \leq (ra_{scene} + \Delta ra)^2 \end{aligned} \quad (32)$$

In Equation (32), all constraints in Equation (20) are fully converted into linear calculation on  $\mathbf{X}_R$  and  $\mathbf{x}_R$ . Therefore, the cost function and all constraints are convex. By substituting Equation (32) into Equation (31), we obtain the following SDP model:

$$\begin{aligned}
 & \min_{\mathbf{X}_R, \mathbf{x}_R} \operatorname{tr} \left\{ \begin{bmatrix} \mathbf{X}_R & \mathbf{x}_R \\ \mathbf{x}_R^T & \mathbf{1} \end{bmatrix} \mathbf{E}_R \right\} \\
 & \text{s.t. } \mathbf{X}_R(4,4) = \operatorname{tr}\{\mathbf{X}_R(1:3,1:3)\} - 2\mathbf{s}_0^T \mathbf{X}_R(1:3) + \mathbf{s}_0^T \mathbf{s}_0 \\
 & \begin{bmatrix} \mathbf{X}_R & \mathbf{x}_R \\ \mathbf{x}_R^T & \mathbf{1} \end{bmatrix} \geq 0 \\
 & x_{\min} \leq \mathbf{x}_R(1) \leq x_{\max} \\
 & y_{\min} \leq \mathbf{x}_R(2) \leq y_{\max} \\
 & z_{\min} \leq \mathbf{x}_R(3) \leq z_{\max} \\
 & R_{near}^2 \leq \operatorname{tr}\{\mathbf{X}_R(1:3,1:3)\} - 2\mathbf{s}_{\eta_c}^T \mathbf{x}_R(1:3) + \mathbf{s}_{\eta_c}^T \mathbf{s}_{\eta_c} \leq R_{far}^2 \\
 & (ra_{scene} - \Delta ra)^2 \leq \operatorname{tr}\{\mathbf{X}_R(1:3,1:3)\} \leq (ra_{scene} + \Delta ra)^2
 \end{aligned} \tag{33}$$

According to reference [31], the solution to the above SDP problem is  $\hat{\mathbf{X}}_R, \hat{\mathbf{x}}_R$ , where the rank of  $\hat{\mathbf{X}}_R$  is  $m$ . When  $m$  satisfies the condition  $m(m+1) \leq 2 \cdot equ$ , where  $equ$  is the number of equality constraints in the SDP problem, the optimal solution of the SDP problem coincides with the global optimal solution of the PRDOA localization model. In Equation (33), the number of equality constraints is 1, making the rank of matrix  $\hat{\mathbf{X}}_R$  be 1, which verifies that the optimal solution  $\hat{\mathbf{x}}_R(1:3)$  of Equation (33) corresponds to the estimated position  $\mathbf{u}$  of the RFI source.

For the SDP problem in Equation (33), there are established algorithms to solve for the global optimal solution, such as Sedumi [32] and SDPT3 [33]. In this paper, the Sedumi solver is used to solve this problem.

### 3.3. Estimation of the Pulse Interval Sum During the SAR Non-Reception Time

According to Equation (16), the PRDOA estimate for the  $n$ th RFI pulse uses the sum of the PRIs  $\sum_{i=0}^{n-1} T_i$  as a known parameter. However, RFI signals cannot be received during the SAR transmitting window and the idle time. This period is defined as the SAR non-reception time. During this period, the sum of the PRIs of the RFI signal  $\sum_{i=0}^{n-1} T_i$  is unknown, requiring the design of an estimation algorithm.

Assume that the SAR raw echo detects RFI signals from the  $X$ th to the  $Y$ th frame. In this scenario, the azimuth and range times of the last RFI pulse in frame  $x - 1$  are denoted as  $\eta_z^{x-1}$  and  $\tau_z^{x-1}$ , respectively, while those of the first RFI pulse in frame  $x$  are  $\eta_{z+y}^x$  and  $\tau_{z+y}^x$ . Here,  $y$  represents the number of RFI pulses occurring during the SAR non-reception time between the  $(x - 1)$ th and  $x$ th frames. The relationships between these parameters are shown in Figure 5.

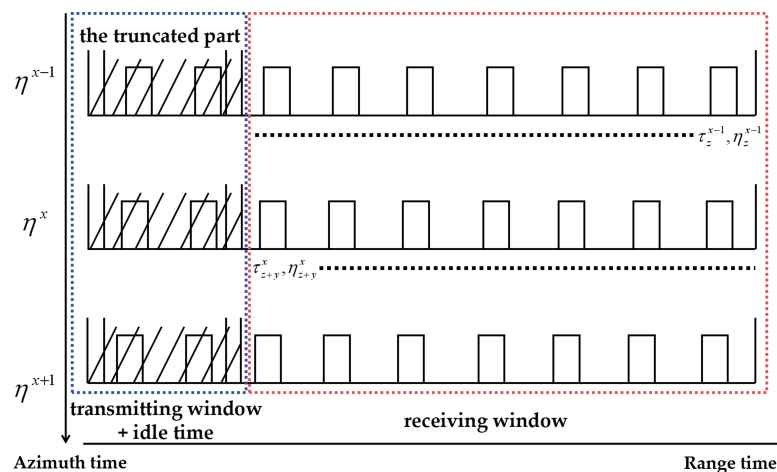


Figure 5. Reception of RFI signals during SAR operation.

Using Equation (16), the total PRI  $T_y$  during the SAR non-reception time between the  $(x - 1)$ th and  $x$ th frames can be derived as shown in Equation (34).

$$T_y = \left( \tau_{z+y}^x + \eta_{z+y}^x \right) - \left( \tau_z^{x-1} + \eta_z^{x-1} \right) - \left( R_{z+y}^r - R_z^r \right) / c = \sum_{n=0}^{y-1} T_n \quad (34)$$

Analysis of Equation (34) reveals that  $T_y$  is mainly influenced by the variation in slant range at the same instant. The duration of the SAR non-reception time is always shorter than the PRI of SAR. For spaceborne SAR, the minimum PRF is no less than 1000 Hz, implying a maximum PRI of 1 ms. It means that the satellite moves approximately 7 m or less during the SAR non-reception time, while the slant range of targets within the swath typically ranges from 500 km to 1000 km. Thus, the slant range of the RFI source remains almost constant during the SAR non-reception time. Therefore, the total PRI  $T_y$  during the SAR non-reception time can be estimated as shown in Equation (35).

$$T_y \approx \left( \tau_{z+y}^x + \eta_{z+y}^x \right) - \left( \tau_z^{x-1} + \eta_z^{x-1} \right) \quad (35)$$

From Equation (35), the estimation of  $T_y$  only depends on the azimuth and range times of the last RFI pulse in the  $(x - 1)$ th frame and the first RFI pulse in the  $x$ th frame. Therefore, the accuracy of  $T_y$  estimation is entirely determined by the algorithm error presented in Section 3.1. Even if the PRI or pulse width exhibits jitter or the RFI pulse satisfies the case 3 mentioned in Section 3.1, as long as the algorithm in Section 3.1 provides high estimation accuracy, the estimation of  $T_y$  will be right.

We design 41 frames of simulated LFM signals to validate the effectiveness of the algorithm presented in this section. A window function truncates the signals, with the portions outside the window considered RFI pulses arriving during the SAR non-reception time. The  $T_y$  for 40 non-reception times needs to be estimated. All signal pulses have identical bandwidths, while their pulse widths and PRIs vary randomly.

Figure 6 illustrates examples of the time-frequency diagrams for the simulated signals and the errors between the estimated and actual  $T_y$ . From the time-frequency diagram in Figure 6a, it can be observed that some pulses exhibit reduced bandwidths, indicating that their pulse widths exceed the length of the receiving window or that the pulse onset times are near the window edges. Figure 6b shows that the  $T_y$  estimation errors are all within 20 ns, demonstrating high accuracy in estimating the sum of PRIs during the non-reception period for the simulated signals.

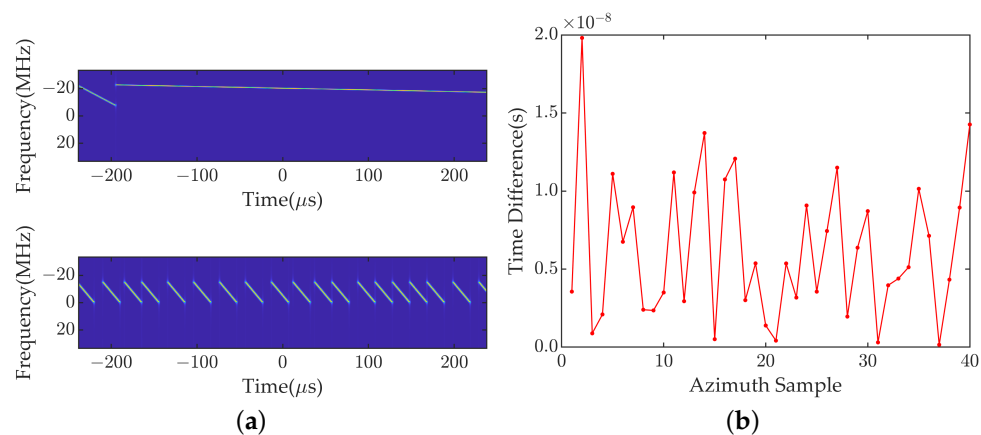


**Figure 6.** Estimation of the total interval of RFI pulses  $T_y$  during the simulated SAR non-reception time: (a) Example of the time-frequency diagram of the simulated signal; (b) Estimation error of the  $T_y$ .

### 3.4. Localization Error Analysis and CRLB

We complete the derivation of the PRDOA localization model by analyzing the bias and covariance of the localization results. Taking the differential of both sides of Equation (16) and rearranging, we obtain:

$$\left[ \frac{(\mathbf{u} - \mathbf{s}_n)^T}{R_n^{ro}} - \frac{(\mathbf{u} - \mathbf{s}_0)^T}{R_0^{ro}} \right] d\mathbf{u} = \Delta r_{n0} - c(Tdn + ndT) + \frac{(\mathbf{u} - \mathbf{s}_n)^T}{R_n^{ro}} d\mathbf{s}_n - \frac{(\mathbf{u} - \mathbf{s}_0)^T}{R_0^{ro}} d\mathbf{s}_0 \quad (36)$$

Here,  $T$  represents the mean PRI of the RFI signal. The expectation of Equation (36) yields the bias of PRDOA localization estimate, which is related to the measurement bias of PRDOA, the PRI measurement bias of RFI, and the satellite orbit bias. Based on assumptions A1 and A2, and the results from Section 3.1, the biases of the three parameters' measurements mentioned above all asymptotically approach zero; thus, the RFI locating estimator based on PRDOA is asymptotically unbiased. The localization method proposed is based on MLE approximation and does not depend on the probability distribution of the measurement noise of PTOA.

Multiplying Equation (36) by its transpose and taking the expectation, we obtain the covariance matrix of the PRDOA localization results:

$$\text{cov}(\mathbf{u}) = G^{-1} \left[ E(\alpha^2) + G_n E(d\mathbf{s}_n d\mathbf{s}_n^T) G_n^T + G_0 E(d\mathbf{s}_0 d\mathbf{s}_0^T) G_0^T \right] G^{-T} \quad (37)$$

where,

$$\begin{aligned} \alpha &= \Delta r_{n0} - c(Tdn + ndT) \\ G_n &= \frac{(\mathbf{u} - \mathbf{s}_n)^T}{R_n^{ro}} \\ G_0 &= \frac{(\mathbf{u} - \mathbf{s}_0)^T}{R_0^{ro}} \\ G &= \left[ (G_n - G_0)^T (G_n - G_0) \right]^{-1} (G_n - G_0)^T \end{aligned} \quad (38)$$

By calculating the trace of the covariance matrix  $\text{cov}(\mathbf{u})$ , we can obtain the mean squared error (MSE) of the RFI localization results. Taking the square root of the MSE yields the root mean squared error (RMSE). Based on Assumption A1, it can be determined that the MSE is influenced by factors such as the RFI source position  $\mathbf{u}$ , satellite orbit, PRDOA measurement error, the PRI of RFI, and the number of RFI pulses received.

From the analysis in Section 3.3, we know that the number of RFI pulses received by the SAR is related to the RFI signal reception duration, the SAR receiving window length, and the pulse repetition frequency (PRF). In practical processing, only one RFI pulse from each frame of SAR echo data is generally selected for localization calculation; thus, only SAR's PRF needs to be considered. Changes in the parameters mentioned above directly affect the RFI source localization error.

The lower bounds of MSE and RMSE are determined by the Cramér–Rao lower bound (CRLB), with the Jacobi matrix defined as follows:

$$\frac{\partial \mathbf{R}}{\partial \mathbf{u}} = \left[ \frac{\partial R_{10}}{\partial \mathbf{u}}, \frac{\partial R_{20}}{\partial \mathbf{u}}, \dots, \frac{\partial R_{N0}}{\partial \mathbf{u}} \right]^T \quad (39)$$

where,

$$\frac{\partial R_{n0}}{\partial \mathbf{u}} = \frac{\partial R_{rx}^n}{\partial \mathbf{u}} - \frac{\partial R_{rx}^0}{\partial \mathbf{u}} = \frac{(\mathbf{u} - \mathbf{s}_n)^T}{\|\mathbf{u} - \mathbf{s}_n\|} - \frac{(\mathbf{u} - \mathbf{s}_0)^T}{\|\mathbf{u} - \mathbf{s}_0\|} \quad (40)$$

Using the Jacobi matrix, we can compute the Fisher information as follows:

$$\text{FIM}_{\mathbf{u}} = \frac{\partial \mathbf{R}^T}{\partial \mathbf{u}} \mathbf{Q}_{\mathbf{R}}^{-1} \frac{\partial \mathbf{R}}{\partial \mathbf{u}} \quad (41)$$

Taking the inverse of the Fisher information yields the CRLB for RFI source localization. To ensure the units are in meters, we take the square root of the CRLB, yielding the following result:

$$\text{CRLB}_{\mathbf{u}} = \sqrt{\text{FIM}_{\mathbf{u}}^{-1}(1,1) + \text{FIM}_{\mathbf{u}}^{-1}(2,2) + \text{FIM}_{\mathbf{u}}^{-1}(3,3)} \quad (42)$$

## 4. Simulation and Experimental Results

This section validates the proposed method's effectiveness using numerical simulation data and the raw echo data from GF3.

### 4.1. Experimental Results Based on Simulation Data

As discussed in Section 3.4, the error in the PRDOA localization is closely related to the following parameters: RFI source position, PRDOA measurement error, satellite orbit, the PRI of RFI, length of the received RFI signal, and the PRF of SAR. As analyzed in Section 3.1 and 3.3, the pulse width and PRI of RFI pulses jointly determine the completeness of their reception. Considering the complexity of RFI variations in practical scenarios, we simplify the analysis by setting the PRI of all RFI pulses equal to their pulse width and controlling the reception status of RFI signals by adjusting the PRI. To analyze the influence of these parameters on the proposed method and demonstrate its superiority, numerical experiments are conducted by designing a spaceborne single-channel SAR simulation platform and an RFI source. These experiments aim to analyze the proposed algorithm's position accuracy variation under different conditions. The PTOA localization proposed in reference [21] is used as a benchmark, and its CRLB is calculated to verify the improvement in localization accuracy achieved by the proposed method. Table 1 presents the operational parameters of the simulated spaceborne SAR.

**Table 1.** SAR system parameters.

SAR System Parameters	
Parameter Items	Parameters
Carrier Frequency (GHz)	1.26
Average Height (km)	600
Average Speed (m/s)	7563
Viewing Angle (deg)	−32.42
Range beam width (rad)	0.07
Azimuth beam width (rad)	0.0243
Sampling rate (MHz)	90
Receiving window duration (μs)	111.11

Specifically, we conduct 2000 Monte Carlo simulation experiments for each parameter setting, with RMSE as the performance metric. CRLB is used as a benchmark to analyze the experimental results. For computational convenience, in the simulation experiments, the first interference pulse in each frame of the detected RFI signal is selected for localization calculation.



#### 4.1.1. Localization Error for Different Satellite Orbit

To analyze the influence of satellite orbit variation on the PRDOA localization model, the following parameters are fixed: the PRF of SAR = 1700 Hz, the RFI signal reception duration = 4 s, the noise standard deviation  $\sigma_{PRDOA} = 4.24$  m, and the PRI of RFI = 10  $\mu$ s. Two sets of satellite orbit parameters are configured based on these parameters, as shown in Table 2.

**Table 2.** Satellite orbit parameters.

Satellite A		Satellite B	
Parameter Items	Parameters	Parameter Items	Parameters
Semi-major Axis (km)	6978.08	Semi-major Axis (km)	6890.75
Eccentricity	0.0012	Eccentricity	0.0011
Inclination (rad)	1.7071	Inclination (rad)	1.7008
RAAN (rad)	0.1936	RAAN (rad)	3.3079
Argument of Periapsis (rad)	1.5708	Argument of Periapsis (rad)	1.5708
True Anomaly (rad)	0.9731	True Anomaly (rad)	0.0000

The center of the SAR swath is used as the reference point, with  $21 \times 20$  grid points set to correspond to the RFI source locations, distributed within the azimuth  $\in [-8, 8]$  km and the range  $\in [702, 752]$  km for satellite A, whereas the range is  $\in [611, 661]$  km for satellite B. The grid point configuration is shown in Figure 7. We apply both the proposed algorithm and the PTOA method to perform localization for two sets of RFI. The RMSE and CRLB for the proposed method, as well as the CRLB for the PTOA method, are obtained. The results are presented as a 2-D image in Figure 8.

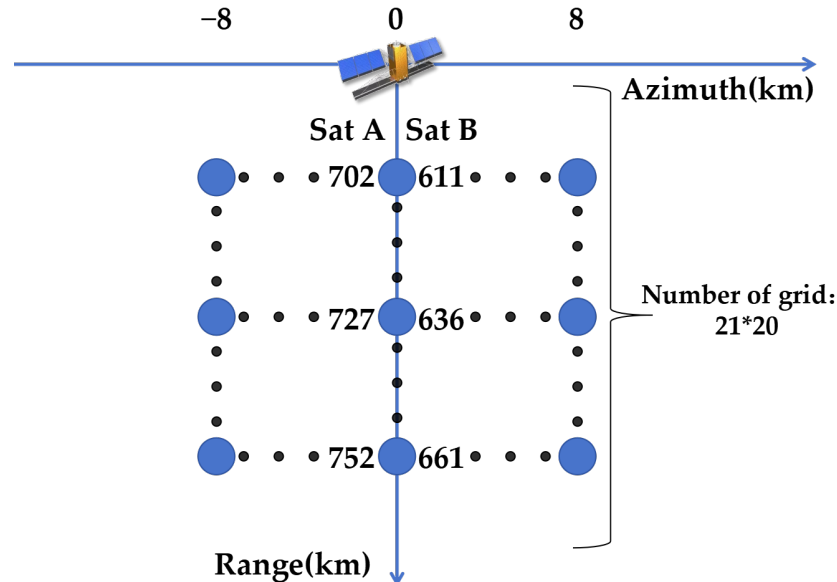


**Figure 7.** Schematic diagram of RFI source grid point setting in the simulation experiment.

The results in Figure 8 show that the trends of RMSE and CRLB obtained by the proposed algorithm are similar, but the CRLB is systematically smaller than the RMSE, which is expected. Additionally, a comparison of Figure 8a,b,d,e reveals that different satellite orbit parameters lead to variations in the distribution of CRLB and RMSE for the proposed algorithm. However, in all cases, the CRLB and RMSE for the proposed algorithm are smaller than the CRLB for PTOA localization.

We plot their range and azimuth distributions to intuitively illustrate the difference between the RMSE and CRLB for the proposed method. Specifically, we calculated the vari-

ations in RMSE and CRLB for the proposed algorithm and the CRLB for PTOA localization at Azimuth = 0 km and Range = 727 km for Satellite A (636 km for satellite B), as shown in Figure 8.

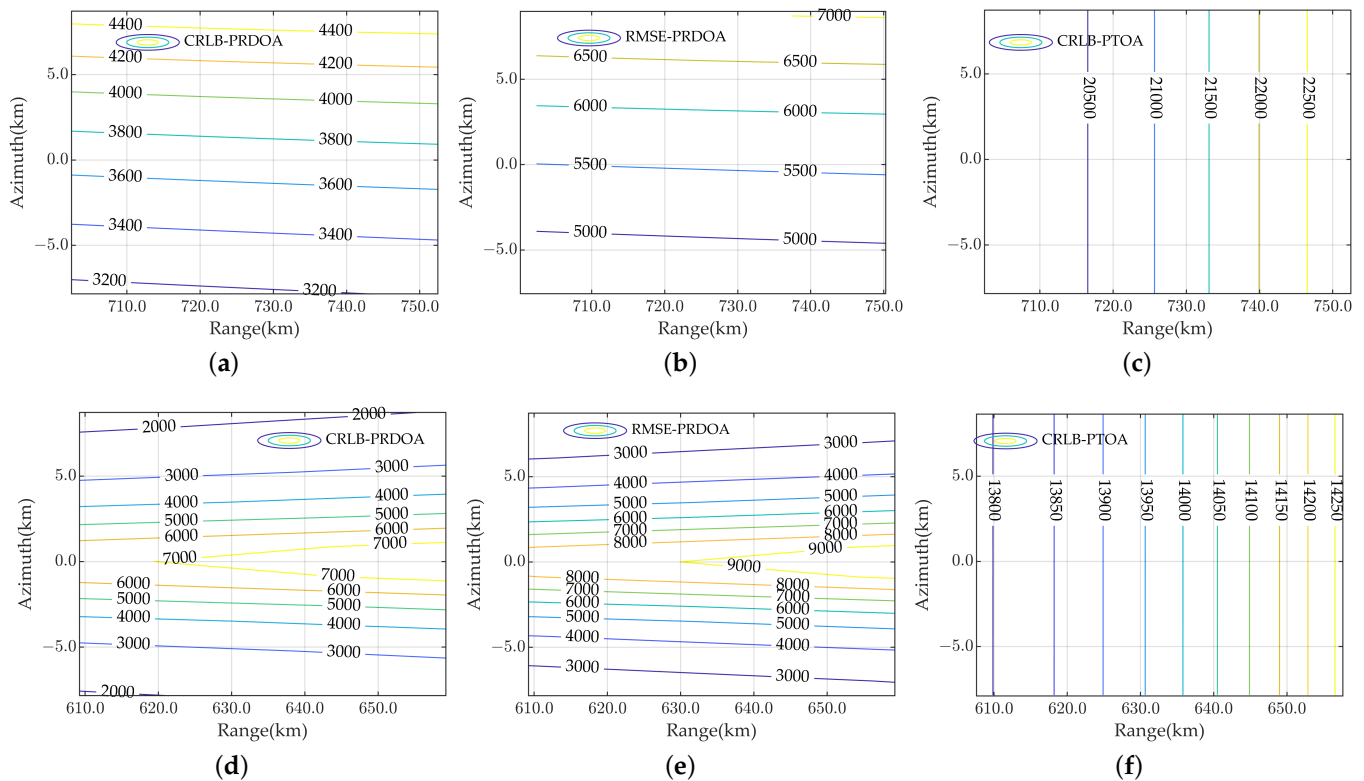


**Figure 8.** 2-D contour plots of the CRLB and RMSE for PRDOA localization, and CRLB for PTOA localization under different satellite orbit parameters: (a–c) Distribution of the CRLB and RMSE for the proposed algorithm and the CRLB for PTOA localization under the Satellite A orbit parameters; (d–f) Distribution of the CRLB and RMSE for the proposed algorithm and the CRLB for PTOA localization under the Satellite B orbit parameters.

The calculation results show that the RMSE of the proposed method is approximately 1.25 to 1.50 times the CRLB. As shown in Figure 9a,c, different satellite orbit parameters lead to different trends in the variation of RMSE and CRLB with changes in the azimuth position. In practical applications, the SAR orbit parameters are determined based on specific observation requirements, so a detailed analysis should be conducted according to the specific scenario. From Figure 9b,d, it can be observed that under both sets of satellite orbit parameters, the CRLB and RMSE of the proposed algorithm increase with the slant range, indicating that in different observation scenarios, the trend that localization error increases as the RFI source moves farther from the satellite is consistent.

The calculations show that the RMSE of the proposed method is approximately  $\frac{1}{4}$  to  $\frac{1}{3}$  of the CRLB of the PTOA localization method, demonstrating a significant improvement in localization accuracy. In the subsequent experiments, satellite A's orbit parameters will be fixed to minimize the influence of orbit parameters.

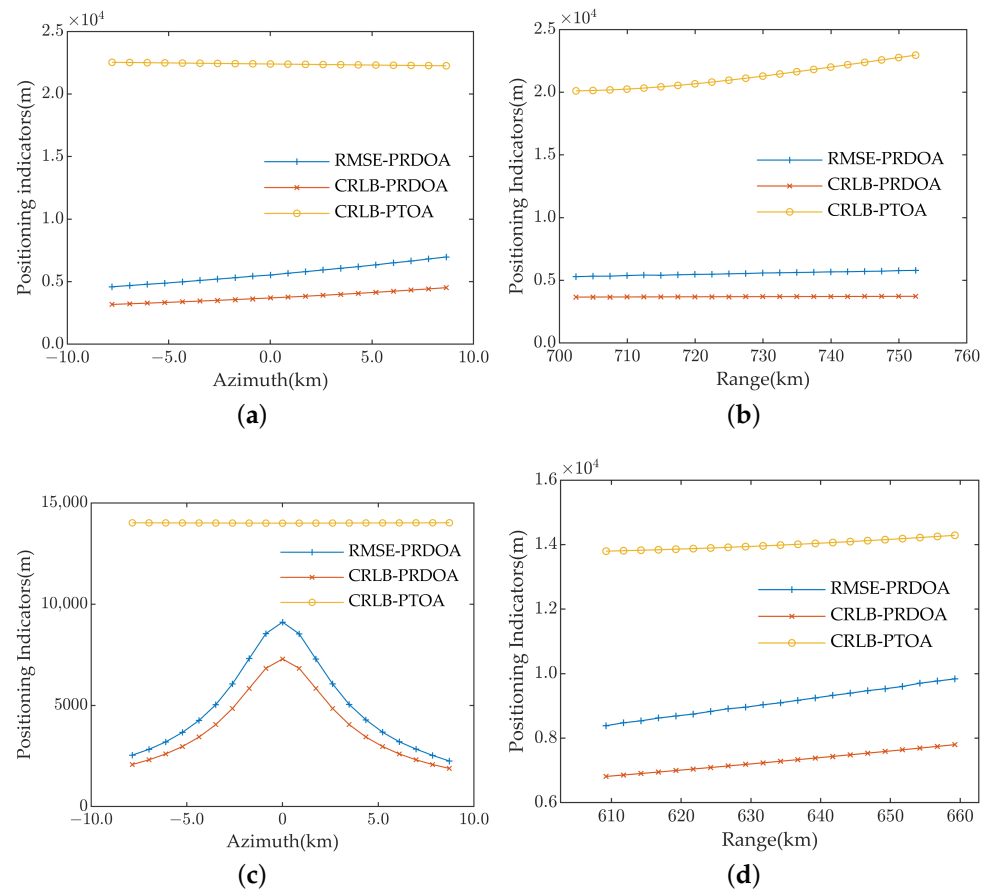


**Figure 9.** Variation in RMSE and CRLB for PRDOA localization and CRLB for PTOA localization with azimuth and range under different satellite orbit parameters: (a,b) Variation in CRLB and RMSE for the proposed algorithm and CRLB for PTOA localization with azimuth and range under Satellite A orbit parameters; (c,d) Variation in CRLB and RMSE for the proposed algorithm and CRLB for PTOA localization with azimuth and range under Satellite B orbit parameters.

#### 4.1.2. Variation in Azimuth and Range Localization Errors at Different Target Points

To analyze the localization errors produced by the proposed algorithm in the azimuth and range directions at target points and their trends with changes in the target location, the same fixed parameters as in Section 4.1.1 are used, and the projections of the results in Figure 9 onto the azimuth and range directions are calculated. The results are shown in Figure 10.

As shown in Figure 10a,b, near the center of the SAR observation region, the azimuth CRLB of PTOA localization is lower than that of the proposed algorithm, indicating that when the RFI source is near the center, PTOA achieves higher azimuth localization accuracy. However, as the RFI source shifts further from the center in the azimuth direction, the azimuth localization error of PTOA increases significantly, while the azimuth CRLB and RMSE of the proposed algorithm remain stable. This suggests that the proposed algorithm provides stable performance for localizing RFI sources across different azimuth positions, maintaining azimuth localization errors within the hundred-meter level.

Figure 10c,d indicate that as the RFI source moves in the range direction, the range RMSE and CRLB of the proposed algorithm are approximately one-third to one-fourth of the range CRLB of PTOA localization, highlighting the clear advantage of the proposed algorithm in range localization performance.

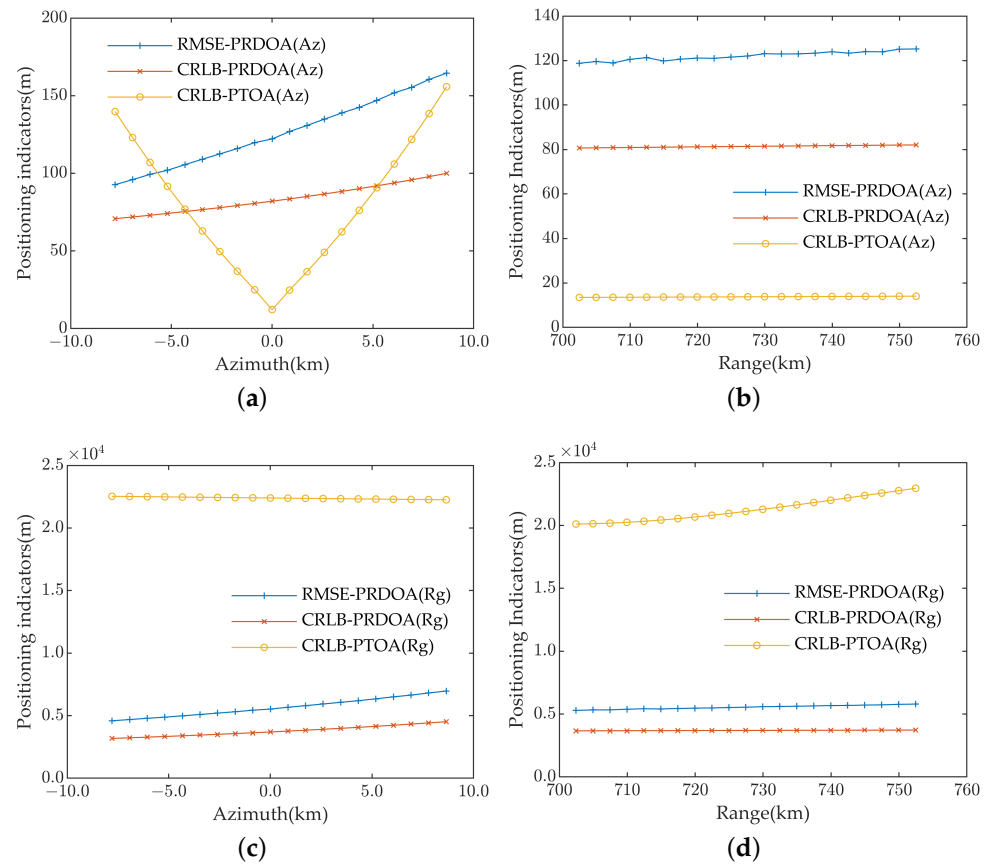


**Figure 10.** Projections of PRDOA and PTOA localization metrics in azimuth and range directions as functions of azimuth and range: (a,b) The azimuth CRLB and RMSE of the proposed algorithm, and the azimuth CRLB of PTOA localization as functions of azimuth and range; (c,d) The range CRLB and RMSE of the proposed algorithm, and the range CRLB of PTOA localization as functions of azimuth and range.

In subsequent experiments, the RFI source will be consistently positioned at the center of the observation area to reduce the impact of position variation and clearly illustrate the relationship between the proposed localization model and different parameters.

#### 4.1.3. Localization Error for Different RFI Signal Reception Durations

To analyze the influence of different RFI signal reception durations on the PRDOA localization model, the following parameters are fixed: the PRF of SAR = 1700 Hz, the noise standard deviation  $\sigma_{PRDOA} = 4.24$  m, and the PRI of RFI = 10  $\mu$ s. With these fixed parameters, the RFI signal reception duration is varied from 2 s to 8 s. We conduct experiments to assess the localization error of the proposed method at different reception durations. The calculated RMSE and CRLB of the proposed method, along with the CRLB of the PTOA localization method, are shown in Figure 11a.

As seen in Figure 11a, both the RMSE and CRLB of the proposed method decrease as the RFI signal reception duration increases. This suggests that longer RFI signal reception durations improve localization accuracy, likely due to the following:

1. A reduction in measurement noise-induced error with longer reception durations.
2. A stabilization of the  $\mathbf{A}_R$  matrix in Equation (23) under longer RFI reception times, ensuring improved localization accuracy [13].

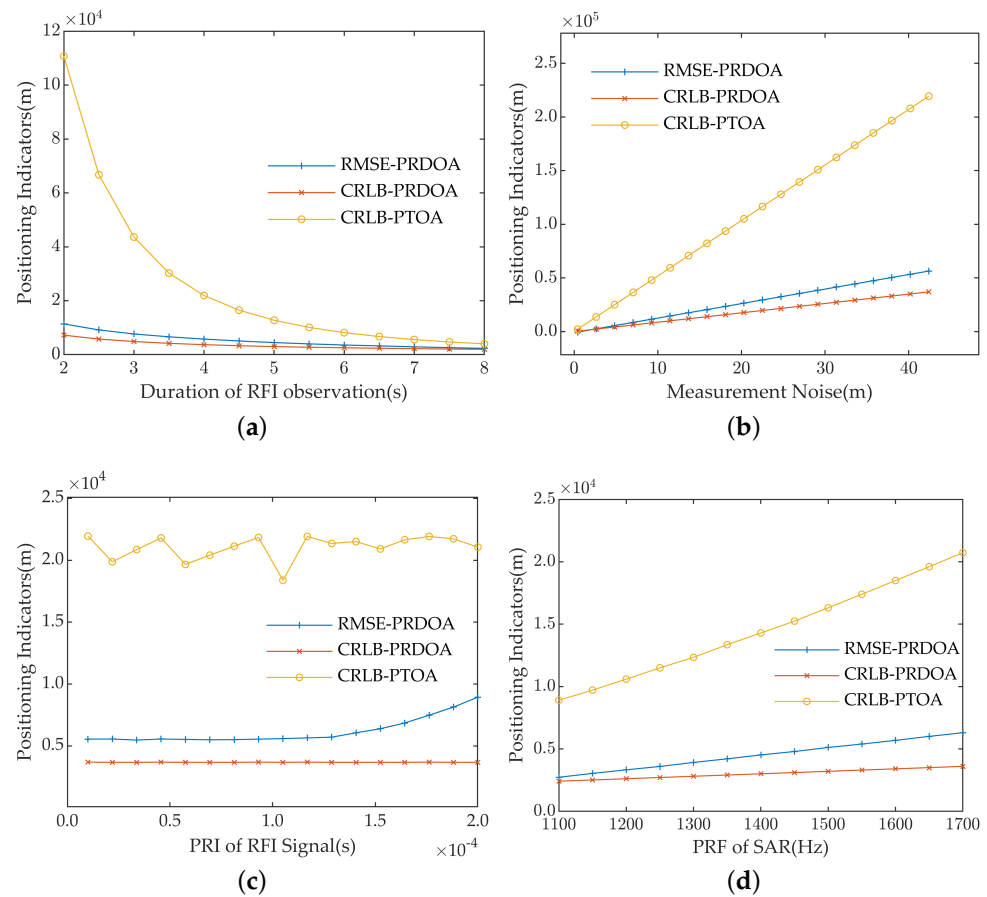


**Figure 11.** Variation in RMSE and CRLB for PRDOA localization and CRLB for PTOA localization with parameter variations: (a) Localization error variations with different RFI signal reception durations; (b) Localization error variations with different noise variances  $\sigma_{PRDOA}$ ; (c) Localization error variations with different PRIs of RFI; (d) Localization error variations with different PRFs of SAR.

From Figure 11a, it can be observed that when the reception duration reaches 8 s or more, the RMSE of the proposed method becomes comparable to the CRLB of the PTOA localization method. When the RFI signal reception duration is less than 7 s, the RMSE of the proposed method remains lower than the CRLB of PTOA localization, with a larger disparity at shorter reception durations. Thus, the proposed method maintains high localization accuracy even with shorter RFI signal reception times.

#### 4.1.4. Localization Error for Different Noise Levels

To analyze the influence of different noise levels on the PRDOA localization model, the following parameters are fixed: the PRF of SAR = 1700 Hz, the RFI signal reception duration = 4 s, and the PRI of RFI = 10  $\mu$ s. With these fixed parameters, we vary the noise variance  $\sigma_{PRDOA}$  from 0.42 m to 42.40 m and conduct experiments to assess the localization error of the proposed method at different measurement noises. The calculated RMSE and CRLB of the proposed method, along with the CRLB of the PTOA localization method, are shown in Figure 11b.

As observed in Figure 11b, both the RMSE and CRLB for the proposed method increase with rising measurement noise. To further analyze this relationship, polynomial fitting is applied, showing that the CRLB and RMSE for the proposed method exhibit a linear relationship with  $\sigma_{PRDOA}$ . Comparing the RMSE of the proposed method with the CRLB of the PTOA localization method reveals that the proposed method shows a less pronounced

increase in localization error as noise increases unlike the PTOA method, indicating superior localization accuracy and stability under high measurement noise.

#### 4.1.5. Localization Error for Different PRIs of RFI

To analyze the influence of different PRIs of RFI on the PRDOA localization model, the following parameters are fixed: the PRF of SAR = 1700 Hz, the RFI signal reception duration = 4 s, and the  $\sigma_{PRDOA} = 4.24$  m. With these fixed parameters, we vary the PRI of RFI from 10  $\mu$ s to 200  $\mu$ s and conduct experiments to assess the localization error of the proposed method. The calculated RMSE and CRLB of the proposed method, along with the CRLB of the PTOA localization method, are shown in Figure 11c.

As seen in Figure 11c, when the RFI PRI is smaller than the SAR receiving window length, neither the RMSE and CRLB of the proposed method nor the CRLB of PTOA localization exhibits any significant increase or decrease with increasing PRI of RFI signal. The reason for the result above is that the SAR does not receive continuous data; rather, it samples in the azimuth direction to generate 2-D image data. Since the localization process typically selects only one pulse containing RFI from each frame for localization calculations, different PRI values have minimal impact on the azimuth and range timing of the RFI pulse selected in each frame. Therefore, the PRI of the RFI signal has little effect on either the proposed algorithm or PTOA localization, when the RFI PRI is smaller than the SAR receiving window length.

When the RFI PRI exceeds the SAR receiving window length, the RMSE of the proposed method increases with PRI. This is because the accuracy of the PRDOA model relies on the algorithm proposed in Section 3.1. As PRI increases, more phase information of RFI pulses is lost outside the single frame, leading to reduced algorithm accuracy and, consequently, increased localization error in the PRDOA model.

Figure 11c also demonstrates that regardless of the completeness of RFI signal reception, the proposed algorithm continues to achieve higher localization accuracy than the PTOA method.

#### 4.1.6. Localization Error for Different PRFs of SAR

To analyze the influence of different PRFs of SAR on the PRDOA localization model, the following parameters are fixed: the PRI of RFI = 10  $\mu$ s, the RFI signal reception duration = 4 s, and the  $\sigma_{PRDOA} = 4.24$  m. With these fixed parameters, we vary the PRF of SAR from 1100 Hz to 1700 Hz and conduct experiments to assess the localization error of the proposed method. The calculated RMSE and CRLB of the proposed method, along with the CRLB of the PTOA localization method, are shown in Figure 11d.

As seen in Figure 11d, the RMSE and CRLB of the proposed method increase with higher SAR PRFs. Polynomial fitting of the data reveals that the RMSE and CRLB of the proposed method exhibit a linear relationship with the  $PRF^{\frac{3}{2}}$ . This phenomenon is due to the correlation between the PRDOA of successive pulses caused by the presence of reference. As the SAR PRF increases, the number of PRDOA elements increases; however, the cumulative timing estimation error of the reference pulses also accumulates, which overshadows the potential improvement in localization accuracy from the increased elements. As a result, the localization performance of the proposed method decreases with higher PRF of SAR.

#### 4.1.7. The Impact of $C_R$ Approximation on PRDOA Localization Accuracy

In Section 3.2.2, the slant range information at the center of the SAR observation area is used as the initial value in the  $C_R$  to simplify the computation. To analyze the impact of  $C_R$  approximation on the accuracy of the PRDOA localization model, the  $21 \times 20$  grid of points under the observation of Satellite A in Section 4.1.1 is selected. The slant range

information between each grid point and Satellite A is calculated and substitutes into the  $C_R$ , and localization is performed using the PRDOA model. The differences between the localization errors of each point based on the real  $C_R$  and those using the approximated  $C_R$  are computed, as shown in Figure 12.

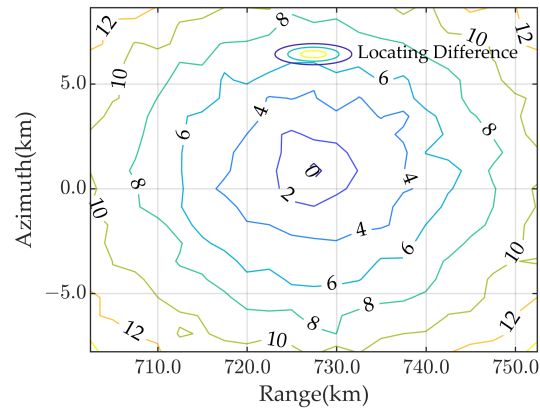


**Figure 12.** Differences between the PRDOA localization errors based on the real  $C_R$  and those using the approximated  $C_R$  for a  $21 \times 20$  grid under the observation of satellite A.

As shown in Figure 12, the maximum difference between the PRDOA localization errors based on the approximated  $C_R$  and the real  $C_R$  does not exceed 15 m. This indicates that the impact of  $C_R$  approximation on the accuracy of the PRDOA localization is minimal, verifying its feasibility.

#### 4.2. Experimental Result Based on Measured Data

In the experiment, GaoFen-3, a high-resolution Earth observation satellite developed by China, is used as the spaceborne SAR platform with an RFI source provided by a simulated radar signal emitter created by Aerospace Information Research Institute, Chinese Academy of Sciences, Beijing, China, as shown in Figure 13.

During the experiment, the RFI source continuously transmitted signals. The experimental location was in Lingshui, Sanya, with the coordinates of the RFI source at (latitude, longitude, height) = (18.413°N, 109.972°E, 15 m). The signal is a frequency-modulated continuous wave (FMCW) with a bandwidth of 15 MHz and a pulse repetition interval of 19  $\mu$ s. Table 3 presents the orbit and imaging parameters of the satellite platform.

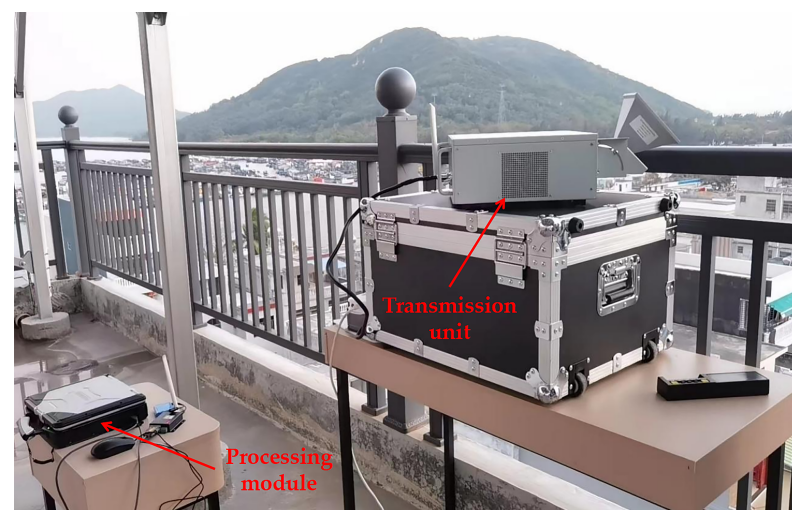


**Figure 13.** Simulated radar RFI source and its deployment environment used in the experiment.

**Table 3.** Orbit and radar parameters of the GF3 satellite.

SAR Parameters		Satellite Orbit Parameters	
Parameter Items	Parameters	Parameter Items	Parameters
Carrier Frequency (GHz)	6978.08	Semi-major Axis (km)	7134.0500
Pulse Width ( $\mu$ s)	0.0012	Eccentricity	0.0016
Band Width (MHz)	1.7071	Inclination (rad)	98.4857
PRF (Hz)	1400	Viewing Angle (deg)	39.1700

Based on the RFI detection and parameter estimation results, we applied matched filtering to the RFI signal for reception time estimation in the SAR echo domain. The matched filtering result for a single RFI frame is shown in Figure 14, demonstrating that the matched filtering effectively focuses the signal energy at the pulse center time, enabling precise estimation of the RFI signal's time information in the SAR echo domain.

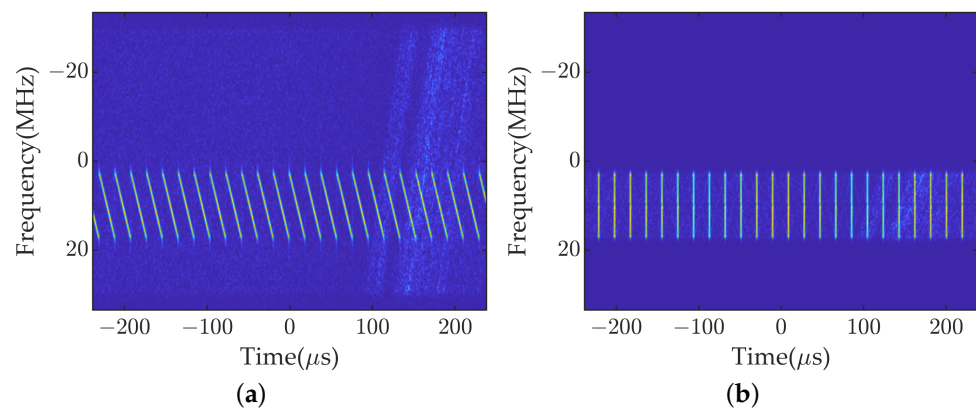


**Figure 14.** Time-frequency images of SAR raw echo with RFI signal and after matched filtering: (a) Time-frequency image of single-frame raw echo with interference signal; (b) Time-frequency image after matched filtering.

Using the estimated time information of the RFI in the SAR echo domain, we selected the first pulse in each frame containing the detected RFI and computed the corresponding PRDOA. The measurement of PRDOA is shown in Figure 15.

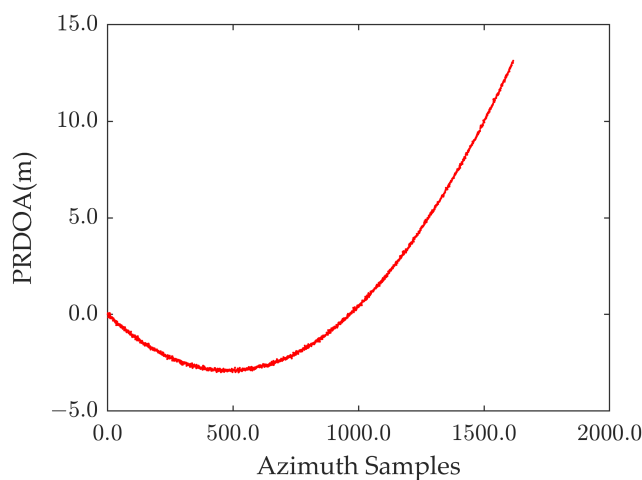


**Figure 15.** PRDOA estimation for each frame in the SAR echo domain with RFI signal.

Using the measured PRDOA, we constructed an optimization model from Equation (33) to obtain the localization results. Additionally, we computed the CRLB value for the same scene using the PTOA localization method. The results of both algorithms are shown in Table 4.



It is evident that the proposed method significantly improves localization accuracy compared to the PTOA method, achieving a total localization error of 7.9874 km and an azimuth error of 350.03 m, both lower than the CRLB of PTOA, closely matching the simulated performance of the proposed method.

**Table 4.** The result of RFI source localization with PTOA and PRDOA method.

PRDOA Localization with SDR Method		PTOA Localization	
Parameter Items	Parameters	Parameter Items	Parameters
Localization Error (km)	7.9874	Localization CRLB (km)	26.6006
Azimuth Error (m)	350.03	Azimuth CRLB (m)	378.54
Range Error (km)	7.9835	Range CRLB (km)	26.5979

In summary, the proposed method meets the high accuracy requirements for locating the RFI source with the spaceborne single-channel SAR, achieving an estimation error of less than 10 km.

## 5. Discussion

In Section 4, simulation experiments and empirical validation using GF3 data are conducted, and based on the covariance analysis of the PRDOA localization model in Section 3.4, we evaluate the impact of various factors on the positioning accuracy of the proposed method while keeping other parameters fixed, with the PTOA model from reference [21] used for comparison.

As shown in Figures 8–11, the RMSE of the proposed algorithm under various simulation conditions is nearly 1.50 times the CRLB. From the analysis in Section 3.2.3, it is evident that the convex optimization problem in Equation (33) aligns with the global optimal solution of Equation (21). This ensures that the localization of the proposed algorithm can closely approach the error lower bound of the PRDOA model.

Further observation of Figures 8–11 and Table 4 reveals that the proposed algorithm improves the localization accuracy by 3 to 4 times compared to the PTOA model under various simulation conditions and real-world scenarios. Moreover, Figures 8 and 9 illustrate that the CRLBs for the PRDOA and PTOA models exhibit different trends as the RFI source distribution varies across the azimuth and range grid points. This phenomenon arises due to the differences in the algebraic relationships between the two models and the RFI source location. In reference [21], the PTOA for the  $n$ th RFI pulse is determined by its emission time  $t_n^{to}$ , the time reference, the RFI source location  $\mathbf{u}$ , and the satellite position  $\mathbf{s}$ . However, as seen in Equations (6) and (15), the PRDOA in the proposed method is only dependent on  $\mathbf{u}$  and  $\mathbf{s}$ . The difference in these algebraic relationships causes the performance of the two localization models to vary differently with changes in the RFI source position and the localization accuracy magnitudes.

As shown in Figure 10, the CRLB of the PRDOA model exhibits a significant difference in the projection magnitudes along the azimuth and range directions, with the former being of the order of hundreds of meters and the latter of the order of kilometers. To investigate the cause of this difference, we set three grid points in both the azimuth and range directions as RFI sources using the simulated single-channel SAR with Satellite A orbit and parameters the same as in Section 4.1.1 for illustrative analysis, as shown in Figure 16.

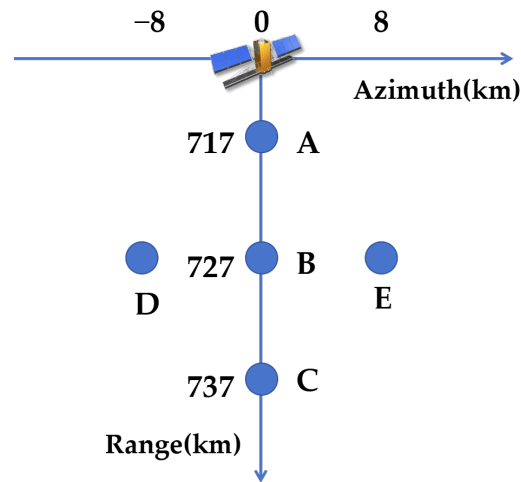


**Figure 16.** Schematic of the RFI source at three grid points in the azimuth or range direction.

The PRDOA of points A to E is calculated, and the results are shown in Figure 17.

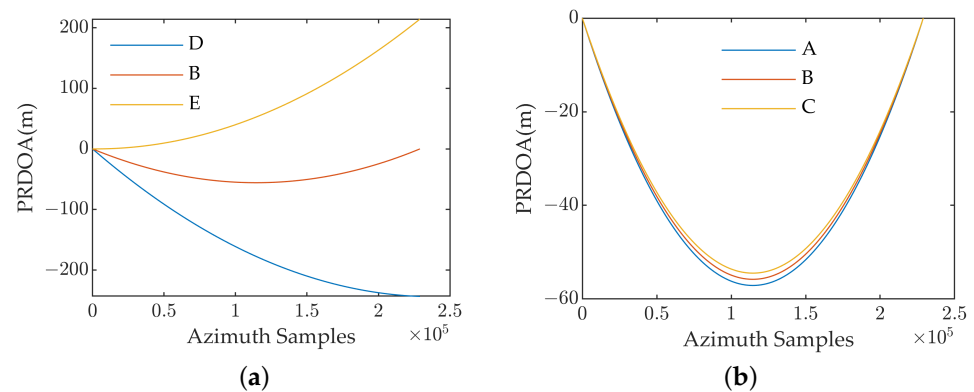


**Figure 17.** PRDOA of three points in the same azimuth or range direction: (a) PRDOA of three points in the same range direction; (b) PRDOA of three points in the same azimuth direction.

By comparing Figure 17a,b, it can be observed that the PRDOA differences among points D, B, and E in the same range direction are much larger than those among points A, B, and C in the same azimuth direction, which indicates that the PRDOA is more sensitive to positional changes of the RFI source in the azimuth direction. As a result, the positioning error projection in the azimuth direction is smaller than in the range direction.

From the simulation or experimental results presented in Section 4, we can conclude that the PRDOA model and SDR-solving method proposed in this paper can achieve high localization accuracy. However, it is important to note that the PRDOA processing assumes that the SAR can continuously receive RFI signals. In practice, RFI signals may exhibit scanning characteristics, leading to cases where some RFI signals are not received or detected while the SAR receiving window is active. If several RFI pulses are lost within a single SAR frame, as discussed in Section 3.3, the onboard SAR moves less than 10 m, and the slant range can be approximated as unchanged. Therefore, the method outlined in Section 3.3 can be used to estimate the range time  $\tau$  for undetected RFI pulses. If a series of consecutive frames in the SAR echo are lost without receiving any RFI signals, the corresponding data cannot be processed by the PRDOA model.

Additionally, due to the complex modulation phase changes in signals transmitted by communication sources, such as Orthogonal Frequency Division Multiplexing, applying this algorithm to locate such RFI sources is more challenging. Therefore, we assume the RFI

source is a radar source in this study. Future work will further analyze these limitations and extend the applicability of the proposed algorithm.

## 6. Conclusions

This paper proposes a spaceborne single-channel SAR RFI source localization model based on PRDOA. First, a geometric model for spaceborne single-channel SAR and the ground-based RFI source is established, along with an RFI signal model. The reception times of RFI pulses in the SAR echo domain are estimated using a matched filtering method. These are then used to construct a PRDOA localization model, which includes the RFI source position information. Given the non-convexity of the model, the WLS equation is used to approximate the localization model, and an SDR method is introduced to transform the model into a convex optimization problem. Theoretical analysis shows that the optimal solution of the approximated convex optimization model is consistent with the results of the PRDOA localization model.

Next, the bias, covariance, and CRLB of RFI source localization based on the PRDOA model are studied, and the method is compared with the PTOA-based localization. Numerical experiments and real data validation are conducted. The results demonstrate that the proposed method can achieve localization accuracy at the kilometer level and azimuth accuracy at the hundred-meter level, with the overall localization accuracy significantly surpassing that of the PTOA method.

It is worth noting that when the RFI signal cannot be fully received by the SAR receiving window, the localization error increases. Additionally, the algorithm has limitations when dealing with RFI sources as communication sources and when there are losses of RFI signals over multiple SAR frames. Future work will focus on addressing these three issues.

**Author Contributions:** Conceptualization, J.W. and B.H.; methodology, J.W.; validation, J.W., J.X., D.Y., J.H. and Y.F.; formal analysis, J.W. and J.X.; investigation, J.W.; resources, J.W., J.X. and B.H.; data curation, J.W., D.Y. and J.S.; writing—original draft preparation, J.W.; writing—review and editing, J.W., B.H., J.X., D.Y. and S.Z.; supervision, B.H. and J.X.; project administration, B.H.; funding acquisition, B.H., J.X. and J.W. All authors have read and agreed to the published version of the manuscript.

**Funding:** This research was funded by the National Natural Science Foundation of China (no.62131019), Key Laboratory of Target Cognition and Application Technology under Grant 2023-CXPT-LC-005, and Foundation Enhancement Research Project (no.E4M40802).

**Data Availability Statement:** The raw data supporting this article will be available upon request.

**Acknowledgments:** We would like to thank the reviewers for their helpful comments.

**Conflicts of Interest:** The authors declare no conflicts of interest.

## References

1. Cao, C.; Bao, L.; Gao, G.; Liu, G.; Zhang, X. A Novel Method for Ocean Wave Spectra Retrieval Using Deep Learning from Sentinel-1 Wave Mode Data. *IEEE Trans. Geosci. Remote Sens.* **2024**, *62*, 4204016. [[CrossRef](#)]
2. Zhang, X.; Gao, G.; Chen, S.W. Polarimetric Autocorrelation Matrix: A New Tool for Joint Characterizing of Target Polarization and Doppler Scattering Mechanism. *IEEE Trans. Geosci. Remote Sens.* **2024**, *62*, 5213522. [[CrossRef](#)]
3. Zhang, C.; Zhang, X.; Gao, G.; Lang, H.; Liu, G.; Cao, C.; Song, Y.; Guan, Y.; Dai, Y. Development and application of ship detection and classification datasets: A review. *IEEE Geosci. Remote Sens. Mag.* **2024**, *12*, 12–45. [[CrossRef](#)]
4. Zhu, X.X.; Montazeri, S.; Ali, M.; Hua, Y.; Wang, Y.; Mou, L.; Shi, Y.; Xu, F.; Bamler, R. Deep learning meets SAR: Concepts, models, pitfalls, and perspectives. *IEEE Geosci. Remote Sens. Mag.* **2021**, *9*, 143–172. [[CrossRef](#)]
5. Tao, M.; Lai, S.; Li, J.; Su, J.; Fan, Y.; Wang, L. Extraction and mitigation of radio frequency interference artifacts based on time-series Sentinel-1 SAR data. *IEEE Trans. Geosci. Remote Sens.* **2021**, *60*, 1–11. [[CrossRef](#)]

6. Huang, Y.; Chen, Z.; Wen, C.; Li, J.; Xia, X.G.; Hong, W. An efficient radio frequency interference mitigation algorithm in real synthetic aperture radar data. *IEEE Trans. Geosci. Remote Sens.* **2022**, *60*, 1–12. [[CrossRef](#)]
7. Shen, J.; Han, B.; Pan, Z.; Li, G.; Hu, Y.; Ding, C. Learning time–frequency information with prior for SAR radio frequency interference suppression. *IEEE Trans. Geosci. Remote Sens.* **2022**, *60*, 1–16. [[CrossRef](#)]
8. Rosenberg, L.; Gray, D.A. Constrained fast-time STAP for interference suppression in multichannel SAR. *IEEE Trans. Aerosp. Electron. Syst.* **2013**, *49*, 1792–1805. [[CrossRef](#)]
9. Hu, F.; Wu, L.; Li, J.; Peng, X.; Zhu, D.; Cheng, Y. RFI localization in synthetic aperture interferometric radiometers based on sparse Bayesian inference. *Int. J. Remote Sens.* **2017**, *38*, 5502–5523. [[CrossRef](#)]
10. Trinh-Hoang, M.; Viberg, M.; Pesavento, M. Partial relaxation approach: An eigenvalue-based DOA estimator framework. *IEEE Trans. Signal Process.* **2018**, *66*, 6190–6203. [[CrossRef](#)]
11. Ho, K. Bias reduction for an explicit solution of source localization using TDOA. *IEEE Trans. Signal Process.* **2012**, *60*, 2101–2114. [[CrossRef](#)]
12. Doğançay, K. Bearings-only target localization using total least squares. *Signal Process.* **2005**, *85*, 1695–1710. [[CrossRef](#)]
13. Chan, Y.T.; Ho, K.C. A simple and efficient estimator for hyperbolic location. *IEEE Trans. Signal Process.* **1994**, *42*, 1905–1915. [[CrossRef](#)]
14. Weiss, A.J. Direct position determination of narrowband radio frequency transmitters. *IEEE Signal Process. Lett.* **2004**, *11*, 513–516. [[CrossRef](#)]
15. Wang, Y.; Sun, G.C.; Wang, Y.; Zhang, Z.; Xing, M.; Yang, X. A high-resolution and high-precision passive positioning system based on synthetic aperture technique. *IEEE Trans. Geosci. Remote Sens.* **2022**, *60*, 1–13. [[CrossRef](#)]
16. Harel, D. X Marks the Spot: Identifying MIM-104 Patriot Batteries from Sentinel-1 SAR Multi Temporal Imagery. 2018. Available online: <https://medium.com/@HarelDan/x-marks-the-spot-579cdb1f534b> (accessed on 5 February 2025).
17. Leng, X.; Ji, K.; Kuang, G. Radio frequency interference detection and localization in Sentinel-1 images. *IEEE Trans. Geosci. Remote Sens.* **2021**, *59*, 9270–9281. [[CrossRef](#)]
18. Yu, J.; Li, J.; Sun, B.; Chen, J.; Li, C.; Li, W.; Xu, L. Single RFI localization based on conjugate cross-correlation of dual-channel SAR signals. In Proceedings of the IGARSS 2019—2019 IEEE International Geoscience and Remote Sensing Symposium, Yokohama, Japan, 28 July–2 August 2019; pp. 385–388.
19. Lin, X.H.; Xue, G.Y.; Liu, P. Novel data acquisition method for interference suppression in dual-channel SAR. *Prog. Electromagn. Res.* **2014**, *144*, 79–92. [[CrossRef](#)]
20. Yu, J.; Li, J.; Sun, B.; Jiang, Y.; Xu, L. Multiple RFI sources location method combining two-dimensional ESPRIT DOA estimation and particle swarm optimization for spaceborne SAR. *Remote Sens.* **2021**, *13*, 1207. [[CrossRef](#)]
21. Yang, H.; Yang, J.; Liu, Z. Localizing ground-based pulse emitters via synthetic aperture radar: Model and method. *IEEE Trans. Geosci. Remote Sens.* **2023**, *61*, 5216714. [[CrossRef](#)]
22. Zhou, S.; Hu, G.; Wang, J.; Chen, Q.; Du, J.; Lu, X.; Wang, Z.; Yang, J.; Tan, K.; Gu, H.; et al. RFI Source Localization for SAR: Method and Experiment based on GaoFen-3. In Proceedings of the IGARSS 2024-2024 IEEE International Geoscience and Remote Sensing Symposium, Athens, Greece, 7–12 July 2024; pp. 7943–7947.
23. Tao, M.; Su, J.; Huang, Y.; Wang, L. Mitigation of radio frequency interference in synthetic aperture radar data: Current status and future trends. *Remote Sens.* **2019**, *11*, 2438. [[CrossRef](#)]
24. Selvan, K.; Siemuri, A.; Prol, F.S.; Välisuo, P.; Bhuiyan, M.Z.H.; Kuusniemi, H. Precise orbit determination of LEO satellites: A systematic review. *GPS Solut.* **2023**, *27*, 178. [[CrossRef](#)]
25. Lou, Y.; Dai, X.; Gong, X.; Li, C.; Qing, Y.; Liu, Y.; Peng, Y.; Gu, S. A review of real-time multi-GNSS precise orbit determination based on the filter method. *Satell. Navig.* **2022**, *3*, 15. [[CrossRef](#)]
26. Lu, W.; Wang, H.; Wu, G.; Huang, Y. Orbit determination for all-electric GEO satellites based on space-borne GNSS measurements. *Remote Sens.* **2022**, *14*, 2627. [[CrossRef](#)]
27. Feng, Y.; Han, B.; Wang, X.; Shen, J.; Guan, X.; Ding, H. Self-Supervised Transformers for Unsupervised SAR Complex Interference Detection Using Canny Edge Detector. *Remote Sens.* **2024**, *16*, 306. [[CrossRef](#)]
28. Liu, Z.; Liao, G.; Yang, Z. Time variant RFI suppression for SAR using iterative adaptive approach. *IEEE Geosci. Remote Sens. Lett.* **2013**, *10*, 1424–1428. [[CrossRef](#)]
29. Tao, J.W.; Yang, C.Z.; Xu, C.W. Estimation of PRI stagger in case of missing observations. *IEEE Trans. Geosci. Remote Sens.* **2020**, *58*, 7982–8001. [[CrossRef](#)]
30. Mardia, H. New techniques for the deinterleaving of repetitive sequences. In Proceedings of the IEE Proceedings F (Radar and Signal Processing), 1989; Volume 136, pp. 149–154. Available online: <https://digital-library.theiet.org/doi/10.1049/ip-f-2.1989.0025> (accessed on 5 February 2025).
31. Barvinok, A.I. Problems of distance geometry and convex properties of quadratic maps. *Discret. Comput. Geom.* **1995**, *13*, 189–202. [[CrossRef](#)]

- 
32. Strum, J. *A Matlab Toolbox for Optimization over Symmetric Cones, Using SEDUMI 1.02 (Ver. 1.05)*; Taylor and Francis Ltd.: Oxford, UK, 2001.
  33. Tütüncü, R.H.; Toh, K.C.; Todd, M.J. Solving semidefinite-quadratic-linear programs using SDPT3. *Math. Program.* **2003**, *95*, 189–217. [[CrossRef](#)]

**Disclaimer/Publisher’s Note:** The statements, opinions and data contained in all publications are solely those of the individual author(s) and contributor(s) and not of MDPI and/or the editor(s). MDPI and/or the editor(s) disclaim responsibility for any injury to people or property resulting from any ideas, methods, instructions or products referred to in the content.